Irregular and stepwise behaviour of hydraulic fracturing: insights from linear cohesive crack modelling with maximum stress criterion

A.R. Khoei [a], S.M.S. Mortazavi [a], L. Simoni [b], B.A. Schrefler [b,c,*]

[a] Center of Excellence in Structures and Earthquake Engineering, Department of Civil Engineering, Sharif University of Technology, PO Box. 11365-9313, Tehran, Iran
[b] Department of Civil, Environmental and Architectural Engineering, University of Padua, Via Marzolo, 9, Padova, Italy
[c] Institute for Advanced Study, Technische Universität München, Lichtenbergstrasse 2a, D-85748 Garching b. München, Germany

ABSTRACT

There is growing evidence that fracture advancement in saturated and dry porous media may be smooth or stepwise. In the stepwise behaviour, there are also pressure oscillations in saturated porous materials, as predicted by Biot's theory. The type of behavior depends on the specifications of the problem and material properties. Not all the adopted numerical models are capable of capturing stepwise behaviour. While non-local fracturing models are perfectly adapted to capture the stepwise behaviour, it is shown that cohesive models are also capable to model such a behaviour. In fact, it is necessary to satisfy a consistency condition for the numerical solution; in other words, the fracture advancement/time-stepping algorithm must not impose a constraint on the tip advancement speed. This is peculiar to cohesive models because there the unit of fracture advancement is specified beforehand, while in other models, such as peridynamics, it is an outcome of the analysis. In inhomogeneous media, it can be expected to capture irregular results from hydraulic fracturing (HF); however, homogeneous media can also show such behaviour as presented herein. In this study, the eXtended Finite Element Method (XFEM) is used in conjunction with a cohesive crack model to investigate the stepwise or irregular behaviour of HF in homogeneous saturated porous media both under quasistatic and dynamic conditions. The results clearly show that the extent of irregularity depends directly on the intensity of dynamic effects in the problem. Moreover, fracture forerunning is one of the reasons of the stepwise fracture growth in the solutions. Although the results are obtained by XFEM, the conclusions are not restricted to this particular numerical method, and the findings can provide useful insights into the necessary aspects of the numerical algorithms for dynamic HF modelling.

1. Introduction

So far, the existing literature on Hydraulic Fracturing (HF) has not answered firmly whether the irregular or stepwise fracture propagation in porous media is a real phenomenon or a numerical artefact. We focus our attention on the cohesive fracture model because it is with such a model that the problem of fracture advancement appeared first in the mechanics community (Schrefler et al., 2006). In this context, we also address the problem of consistency in modelling fracture advancement with a cohesive model in saturated homogeneous porous media, especially when the dynamic effects are not negligible. In cohesive models the crack is usually advanced a predetermined unit length per time- or load-step, in case of FEM analysis often taken to be the size of a generic element in the crack-tip area or on the basis of a predetermined

propagation law, e.g. the Paris-type fatigue evolution (Moës and Belytschko, 2002). This can give rise to a peculiar consistency problem, not present in many other fracturing models. For instance, in methods like the lattice/FEM model (Milanese et al., 2016), or in hybrid Peridynamics/FEM models (Ni et al., 2021; Sun et al., 2021a, 2021b), the fracture advancement is an outcome of the procedure, and the crack tip advancement is not chosen by the user. Since the evidenced consistency issue concerns the fracture propagation, it exists also in dry porous media but we concentrate on saturated porous media because of the quantity of data available. There are also other approaches for modeling HF problems; for instance, Nguyen et al., (2017) suggested a cohesive interface element method for HF simulation, which is mesh dependent. The phase field is another mesh-independent method similar to XFEM, however, it cannot model sharp jumps in the field of solution. However, it can be sufficiently accurate for HF modelling if used properly, the

---

Nomenclature

$2h$	Fracture opening	Q	Water injection rate
$\mathbf{B}_\pi$	Matrix of the shape function gradient for the variable $\pi:(u, w)$	S	In situ stress normal to the crack growth direction
		t	Time
$\mathbf{b}$	Body force	$\mathbf{t}_d$	Cohesive traction vector
$\mathbf{D}$	Elastic constitutive matrix	$\mathbf{T}_d$	Tangent modulus matrix of the cohesive traction
$D_{\Gamma_d}(\boldsymbol{x})$	The distance function	$\mathbf{u},\mathbf{U}$	Nodal DOF of displacement
E	Elasticity modulus	$\dot{\mathbf{w}}_w$	The Darcy velocity
f	Correction coefficient for deviation from the cubic law	$\mathbf{M}$, $\mathbf{K}$, $\mathbf{H}$, $\mathbf{C}$	The coefficient matrices of the governing equations
G	Shear modulus	α	The Biot coefficient
G_c	Cohesive fracture energy	ε	Strain
$H_{\Gamma_d}(\boldsymbol{x})$	The step function	$\varphi(\mathbf{x})$	The signed distance function
k	Intrinsic permeability of the porous medium	Γ_d	Discontinuity trajectory
K_S	Bulk modulus of solid grains	μ_w	Dynamic viscosity of water
K_T	Bulk modulus of porous medium	ν	Poisson ratio
k_w	Permeability of water	Ω	Domain of the porous medium
k_{wd}	Permeability of the fracture	ρ	Average density of the medium
L	Crack length	ρ_π	Density of the phase $\pi : (u,s)$
$\mathbf{m}$	The unit vector	σ	Total stress
n	Porosity	σ''	Modified effective stress
n_{Γ_d}	The normal unit vector to the discontinuity	σ_c	Cohesive strength
N_π	Shape functions for the variable $\pi : (u,w)$	$[[\Xi]]$	The difference (or jump) of the variable Ξ at the discontinuity faces
p_w	Pore pressure of water	$\langle \Xi \rangle$	The average of variable Ξ at the discontinuity faces
$\mathbf{p}_w,\mathbf{P}_w$	Nodal DOF of water pressure	$\|\Xi\|$	The Euclidian norm of Ξ

examples of which can be found in the works of Miehe et al. (2015; Wilson and Landis (2016); Zhou et al., (2018). It is evident that each of these numerical methods has pros and cons such that it is not possible to determine the best of all in HF modelling. However, the XFEM model proposed here has been successfully used for various HF and other fracturing problems in porous media (Réthoré et al., 2008; Moham-madnejad and Khoei, 2013a, 2013b; Khoei and Mortazavi, 2020). Furthermore, the concluding remarks of this study are not restricted to the XFEM, and they hold for any other numerical methods with the maximum stress criterion and the linear cohesive crack model.

To avoid confusion, it is first necessary to explain the meaning of smoothness and regularity here. In calculus, a curve is called smooth if (at least) its first-order derivative is continuous. Therefore, stepwise curves with sharp jumps are not smooth. The term stepwise is generally used in this article for curves with single or multiple instances of non-smoothness. Note that the numerical solution of a smooth problem can present a stepwise behaviour that originates from the finite dis-cretization of the solution (Mohammadnejad and Khoei, 2013a; Hage-man et al., 2019; Bai et al., 2020). In this regard, a problem is smooth when its numerical solution converges to a smooth curve if the temporal and spatial discretizations are extremely refined. In contrast, the inherent stepwise behavior does not vanish with refinement and it can work as a criterion to distinguish between the stepwise and smooth behavior. On the other hand, regularity means that the solution is pre-dictable, regardless of converging to a stepwise or smooth solution, ul-timately. In other words, regular solutions follow a particular trend, e.g. linear, exponential, power, etc., that makes it feasible to extrapolate the results with acceptable accuracy. If the solution does not follow a pre-dictable trend, it is called irregular hereafter. This study focusses on the smoothness and regularity of the crack length history. The provided examples show that the regularity and smoothness of the crack length history do not necessarily correlate with each other.

The stepwise and irregular behavior of fracture growth in hetero-geneous media is evidently expected which can originate from the ma-terial properties (Liang et al., 2012; Duan et al., 2020; Zou et al., 2020), the network of preexisting fractures (Zhou and Yang, 2022), or impending microcracks in the fracture process zone (Zhang et al., 2019).

In contrast, analytical or semi-analytical solutions for the advancement of fractures in homogeneous and saturated porous media yield smooth and regular solutions. Note that these solutions ignore crucial dynamic effects, such as wave propagation emanating from fracture advance-ment. Moreover, fluid leakage through the fracture faces is commonly disregarded or considered by very simple approximations in analytical solutions (Geertsma and Haafkens, 1979). For example, consider the asymptotic approach used by Detournay (2016), where the fracture grows smoothly over time. Smoothness is based on the assumption that the solution near the tip of a propagating finite hydraulic fracture is captured by a stationary solution for a semi-finite crack moving at a constant velocity (Lecampion et al., 2018).

But should we assume that such a process is smooth? Several ex-periments show that, at the time scale usually of interest in experiments, it is possible to observe a smooth growth of the fracture. The same ex-periments can be readily reproduced by continuous models; see, e.g., Bunger and Detournay (2008) and Bunger et al., (2013). However, jumps in crack advancement can be observed in dynamic or quasi-static experiments (Sammonds et al., 1989; Pizzocolo et al., 2013; Dong et al., 2019). Such jumps have been reproduced mathematically and numeri-cally in dynamics problems (Tvergaard and Needleman, 1993; Slepyan et al., 2015; Peruzzo et al., 2019b; Ni et al., 2021). Dynamic crack jumps are also foreseen, as presented by Bazant et al., (2014). Furthermore, it is shown that crack forerunning is an undeniable source of stepwise advancement of the main crack in continuum models, and that fore-running increases in dry bodies the overall fracturing speed (Slepyan et al., 2015; Ni et al., 2021). It is a mechanism for a crack to move faster when the steady-state propagation is no longer supported by the body due to a high level of external forces. For saturated bodies in the pres-ence of forerunning, the interaction with waves in the fluid phase in-creases the average fracturing speed even further compared to dry bodies (Ni et al., 2021). Considering the multiscale aspects of the matter and the self-organisation of rupture, there is no such mechanism as a continuous tip velocity (Herrmann, 1990; Tzschichholz and Herrmann, 1995; Peruzzo et al., 2019a). The limits of tip asymptotic are also evi-denced when trying to reproduce the behaviour observed in carefully carried out experiments with hydrogels (O'Keeffe et al., 2018; O'Keeffe,

2019).

Stepwise fracture advancement and ensuing pressure fluctuation have received much attention in the oil industry from the 1980 s on, both in the field and experimentally (Black, 1988; Morita et al., 1990; Fuh et al., 1992; Lhomme et al., 2002; Okland et al., 2002; Lhomme, 2005; Zhang and Chen, 2010; Fisher and Warpinski, 2012; Soliman et al., 2014; De Pater, 2015; Razavi et al., 2016; Trimonova et al., 2017). The problem is also of great economic relevance in fracking operations for their steering (Soliman et al., 2014). Intermittent fracture advancement in saturated formations attracted attention in geophysical observations even earlier (Phillips, 1972; Sibson, 1994; Cox, 1995; Obara et al., 2004; Schwartz and Rokosky, 2007; Burlini and Di Toro, 2008; Beroza and Ide, 2009; Burlini et al., 2009). Without such a behaviour, the nonvolcanic (subduction) tremor and volcanic tremor are difficult to explain.

On the numerical side, most continuum models converge to smooth answers (Hageman et al., 2019; Shi and Liu, 2021); however, an increasing number of continuum models capture stepwise advancement, also. This is certainly the case for nonlocal models, such as those presented by Ni et al. (2021) and Hageman and de Borst (2021). Even if a majority of papers feature continuous behaviour in HF dealing with cohesive zone model, such models can yield stepwise advancement, too; see Cao et al. (2017) for a review. More recent papers that show stepwise behaviour with cohesive zone models in conjunction with FEM are those reported by Arzanfudi and Al-Khoury (2017); Ding et al., (2018); Feng and Gray, (2017); Vahab et al., (2018). So the yet unanswered question arises of why some continuum models with cohesive fracture yield stepwise advancement and pressure fluctuation, while others yield only smooth and regular solutions (Peruzzo et al., 2019b). One reason is whether the employed fracture advancement algorithm satisfies or not from a numerical point of view the consistency condition and from a physical point of view the self-organisation of rupture mentioned above. The second aspect requires that (i) the external drive has a much slower timescale than fracture propagation; and (ii) the increase in external load (drive) is applied only when the internal rearrangement of the fracture is over. Actually, condition (ii) is a consequence of (i), and they constitute a 'quasi-static' simulation. Incidentally, the second requirement also works well in dynamics, as shown by Peruzzo et al., (2019a). Satisfying conditions (i) and (ii) implies that there should be no restriction on the fracture velocity, i.e. algorithmically the fracture advancement rule should always be independent of the crack velocity. This brings us back to the consistency condition, which results in the fact that the adopted algorithm should not limit the fracture advancement speed as shown in the sequel. Another reason for smooth results, as found in this study, is the problem specifications, which will be discussed further in the numerical examples. The paper is organised as follows; in Section 2, we present a review of the governing equations and the numerical method. Further we recall the numerical properties required for a convergent solution and indicate a criterion that the fracture tip advancement / timestep algorithm used in modelling the fracture advancement with cohesive models should satisfy. In Section 3, we present extensive parametric studies for the smooth and irregular behaviour of HF using the XFEM with a linear cohesive crack model, both in dynamics and quasi-statics. Finally, the concluding remarks are given in Section 4.

2. Modelling fracture advancement with cohesive crack model

2.1. Physical Model

Since the physical and numerical models used in this study are the same as those presented in (Mohammadnejad and Khoei, 2013b, 2013a), we only summarise the key points of the relations in this document. Moreover, interested readers can refer to Chan et al., (2022) for more details on the physical model. In fully saturated porous media, it is assumed that the pores of the solid matrix and the fracture space are fully filled with a single wetting phase (w). It is assumed that the bulk porous medium as well as the solid phase are compressible. The modified effective stress vector is then defined as follows.

$$\sigma'' = \sigma + \alpha \mathbf{m} p_w \tag{1}$$

where σ'' is the modified effective stress, σ is the total stress, and p_w is the pore pressure of the fluid phases. The Biot coefficient α is defined as $\alpha = 1 - K_T/K_S \leqslant 1$, in which K_T and K_S are the bulk moduli of the porous medium and the solid grains, respectively. The vector $\mathbf{m}$ denotes the unit vector defined as $\mathbf{m} = \begin{bmatrix} 1 & 1 & 0 \end{bmatrix}^T$ in two-dimensional problems. Taking into account the linear elastic behaviour, the stress–strain relationship of the solid phase can be written as

$$d\sigma'' = \mathbf{D} d\varepsilon \tag{2}$$

where $\mathbf{D}$ denotes the constitutive elastic matrix and ε is the strain vector. According to the averaging theory, the governing equations of the porous media can be derived by multiplying the equation of each phase with its corresponding volumetric fraction and summing them over the domain (Lewis and Schrefler, 1998). On the basis of this theory, the linear momentum balance equation of porous media can be derived as

$$\mathbf{L}^T \sigma + \rho \mathbf{b} - \rho \ddot{\mathbf{u}} = \mathbf{0} \tag{3}$$

in which $\rho = (1-n)\rho_s + (n)\rho_w$ is the average density of the medium, $\mathbf{b}$ is the body force, $\ddot{\mathbf{u}}$ is the acceleration of the solid phase, and $\mathbf{L}$ is the gradient operator defined as

$$\mathbf{L} = \begin{bmatrix} \partial/\partial x & 0 \\ 0 & \partial/\partial y \\ \partial/\partial y & \partial/\partial x \end{bmatrix} \tag{4}$$

The linear momentum balance equations of the fluid phases can be approximated by the generalised Darcy equation as follows.

$$\dot{\mathbf{w}}_w = k_w \left(-\nabla pw + \rho_w (\mathbf{b} - \ddot{\mathbf{u}}) \right) \tag{5}$$

where $\dot{\mathbf{w}}_w$ is the Darcy velocity, $k_w = k/\mu_w$ denotes the permeability of the fluid phase, k is the intrinsic permeability of the porous medium, and μ_w is the dynamic viscosity of the fluid. It should be noted that the relative acceleration of the fluid is not considered in equation (5). This assumption is valid for a wide range of practical problems with low frequency conditions, as described by Zienkiewicz et al., (1980) and Chanet al., 2022). Applying the averaging theory to combine the continuity equation of the solid phase with that of the fluid phase, and substituting equations of the state for each phase, the continuity equations of the fluid phase can be obtained as follows.

$$\left(\frac{\alpha - n}{K_S} + \frac{n}{K_w} \right) \dot{p}_w + \alpha \nabla^T \dot{\mathbf{u}} + \nabla^T \dot{\mathbf{w}}_w = 0 \tag{6}$$

in which $\dot{\mathbf{u}}$ is the solid velocity and n is the porosity. Similarly, the continuity equation of the fluid within the fracture can be considered as

$$\frac{1}{K_w} \dot{p}_w + \nabla^T \dot{\mathbf{u}} + \nabla^T \dot{\mathbf{w}}_w = 0 \tag{7}$$

For simplicity, it is commonly assumed that fluid flow within the fracture can be approximated by the cubic law, which renders the permeability coefficient of the fracture as

$$k_{wd} = \frac{1}{f} \frac{(2h)^2}{12\mu_w} \tag{8}$$

where $2h$ is the opening of the fracture and f is a correction coefficient for deviation from the assumption of ideally smooth and parallel faces. This factor is taken as 1.0 in this study.

In general, there are three modes of failure considered at the tip of the crack. In this study, mode I of the fracture (the pure opening mode) is only considered. In quasi-brittle materials, such as rock and concrete, the size of the nonlinear zone at the fracture tip is not negligible. Hence,

the cohesive crack model is suggested for such materials (Bazant and Planas, 1998). In this model, the stress distribution in the fracture process zone is lumped into a fictitious crack tip segment; therefore, the singularity of stress vanishes at the real crack-tip. The lumped stress can be obtained from a traction-separation law in which the cohesive traction is a function of the jump in the displacement field at both sides of the fracture as follows:

$$\mathbf{t}_d = \mathbf{t}_d([[\mathbf{u}]]) \tag{9}$$

The linearisation of this equation takes the form

$$\mathrm{d}\,\mathbf{t}_d = \mathbf{T}_d\,\mathrm{d}[[\mathbf{u}]] \tag{10}$$

where $\mathbf{t}_d$ is the cohesive traction vector and $\mathbf{T}_d$ is the tangent modulus matrix of the cohesive traction defined by $\mathbf{T}_d = \partial \mathbf{t}_d/\partial[[\mathbf{u}]]$. By arbitrarily denoting the sides of the discontinuity as positive or negative regions, the jump symbol $[[*]] = *^+ - *^-$ is defined as the difference of variable $*$ across the two sides of the fracture. If only mode I fracture is assumed, the shear component of cohesive traction is neglected and the tangential modulus matrix can be obtained as

$$\mathbf{T}_d = \mathbf{n}_{\Gamma_d}\frac{\partial t_{d_n}}{\partial[[u_n]]}\mathbf{n}_{\Gamma_d}^{\mathrm{T}} \tag{11}$$

in which $\mathbf{n}_{\Gamma_d}$ is the normal unit vector to the discontinuity, t_{d_n} is the normal component of the cohesive traction, and $[[u_n]]$ is the crack opening displacement. The quasi-brittle materials usually show a softening behaviour as a result of damage after reaching their maximum strength. The critical opening displacement is defined as the opening displacement where the cohesive traction becomes zero, indicating the traction-free faces behind the real crack-tip. To consider the softening behavior, a linear softening traction-separation law is utilised. This means that the magnitude of cohesive traction varies linearly from zero to the tensile strength, corresponding to the opening displacement from critical value to zero, respectively. This softening behaviour is considered for the loading phase or simply the increasing phase of the aperture. On the other hand, in the unloading phase the cohesive traction is allowed to decrease linearly to a zero-zero state of traction-separation.

2.2. Numerical model

In this section, the spatial discretization of the governing equations is performed using XFEM. It is a well-known numerical method in the field of fracture propagation modelling, in which the discontinuity can be incorporated into the solution independently of the mesh. In this method, the shape functions of the elements bisected by the discontinuity are enriched by some specific functions. The solid-phase displacement and the water pressure are assumed to involve strong and weak discontinuities, respectively. This means that there is a jump in the displacement field across the fracture, but the water pressure field is continuous, in contrast to its gradient (Khoei, 2015). Assuming the general configuration of a fractured medium, as depicted in Fig. 1, the signed distance function can be defined as

$$\varphi(\mathbf{x}) = \|\mathbf{x} - \mathbf{x}^*\|sign\left(\mathbf{n}_{\Gamma_d}\cdot(\mathbf{x} - \mathbf{x}^*)\right) \tag{12}$$

where $\mathbf{x}^*$ is the projection of the point $\mathbf{x}$ on the discontinuity Γ_d, and $\mathbf{n}_{\Gamma_d}$ is the normal vector to Γ_d at the point $\mathbf{x}^*$. The symbol $\|*\|$ represents the Euclidian norm. Then, the distance function is defined as $D_{\Gamma_d}(\mathbf{x}) = |\varphi(\mathbf{x})|$. Another important function to be used as an enrichment function, is the step function as given below.

$$H_{\Gamma_d}(\mathbf{x}) = sign(\varphi(\mathbf{x})) = \begin{cases} +1 & \mathbf{x} \in \Omega^+ \\ 0 & \mathbf{x} \in \Gamma_d \\ -1 & \mathbf{x} \in \Omega^- \end{cases} \tag{13}$$

Incorporation of enrichment functions into the solution involves the introduction of new degrees–of–freedom (DOF), called the enriched DOF, limited only to the nodal points of bisected elements. Accordingly, the displacement field of the solid phase can be approximated within the XFEM framework as follows.

$$\mathbf{u}^h(\mathbf{x}, t) = \sum_{I\in N^{\mathrm{std}}}\mathbf{N}_{u_I}(\mathbf{x})\mathbf{u}_I(t) + \sum_{J\in N^{\mathrm{enr}}}\mathbf{N}_{u_J}(\mathbf{x})\frac{1}{2}\left(H_{\Gamma_d}(\mathbf{x}) - H_{\Gamma_d}(\mathbf{x}_J)\right)\widetilde{\mathbf{u}}_J(t) \tag{14}$$

in which $\mathbf{u}^h$ is the approximation function, $\mathbf{u}_I(t)$ is the nodal displacement, $\widetilde{\mathbf{u}}_J(t)$ is the enriched DOF, and $\mathbf{N}_{u_i}$ represents the standard shape functions from FEM. Note that in order to satisfy the closure of the fracture tip, the nodes in their support which contains the fracture tip are not enriched. The concise form of this equation can be written as

$$\mathbf{u}^h(\mathbf{x}, t) = [\,\mathbf{N}_u(\mathbf{x}) \quad \mathbf{N}_u^{\mathrm{enr}}(\mathbf{x})\,]\cdot\begin{bmatrix}\mathbf{U}(t) \\ \widetilde{\mathbf{U}}(t)\end{bmatrix} = \overline{\mathbf{N}}_u\cdot\overline{\mathbf{U}} \tag{15}$$

where the definition of $\mathbf{N}_u^{\mathrm{enr}}(\mathbf{x})$ can be deduced from equation (14). Moreover, the strain matrix can be obtained as

$$\varepsilon^h(\mathbf{x}, t) = [\,\mathbf{B}_u(\mathbf{x}) \quad \mathbf{B}_u^{\mathrm{enr}}(\mathbf{x})\,]\cdot\begin{bmatrix}\mathbf{U}(t) \\ \widetilde{\mathbf{U}}(t)\end{bmatrix} = \overline{\mathbf{B}}_u\cdot\overline{\mathbf{U}} \tag{16}$$

in which the matrices $\mathbf{B}(\mathbf{x})$ and $\mathbf{B}^{\mathrm{enr}}(\mathbf{x})$ contain the spatial derivatives of the standard and enriched shape functions, defined as $\mathbf{B}(\mathbf{x}) = \mathbf{L}\mathbf{N}_u(\mathbf{x})$ and $\mathbf{B}^{\mathrm{enr}}(\mathbf{x}) = \mathbf{L}\mathbf{N}_u^{\mathrm{enr}}(\mathbf{x})$, respectively.
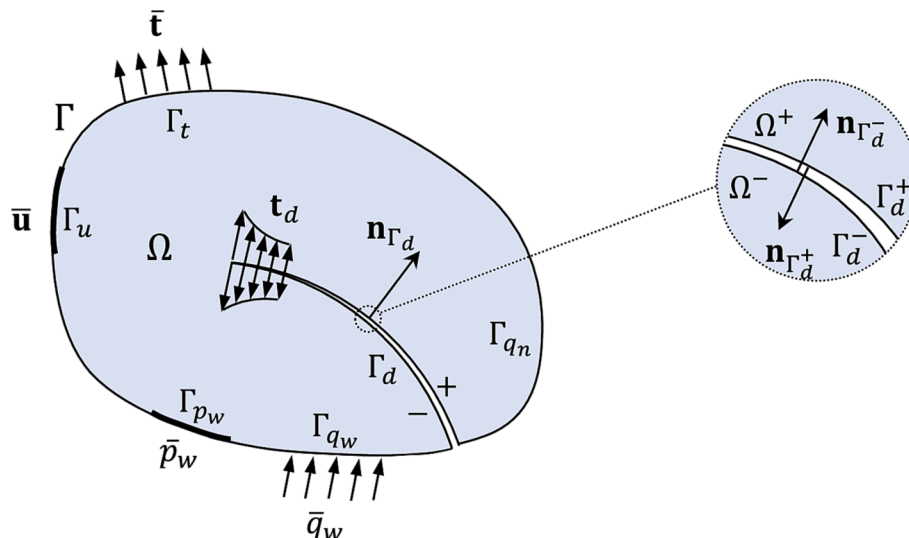

Fig. 1. The schematic geometry of the fractured porous medium.

The approximation form of the fluid pressure can be written using the distance function as

$$
p_w^h(\mathbf{x}, t) = \sum_{I \in N^{\text{std}}} \mathbf{N}_{w_I}(\mathbf{x}) \mathbf{p}_{w_I}(t)
$$
$$
+ \sum_{J \in N^{\text{enr}}} \mathbf{N}_{w_J}(\mathbf{x}) \big(D_{\Gamma_d}(\mathbf{x}) - D_{\Gamma_d}(\mathbf{x}_J)\big) \widetilde{\mathbf{p}}_{w_J}(t)
\tag{17}
$$

in which $\mathbf{p}_{w_I}(t)$ and $\widetilde{\mathbf{p}}_{w_J}(t)$ denote the vectors of standard and enriched DOF, respectively. The nodes in their support which contains the fracture tip are not enriched, since the leakage flux must disappear at the fracture tip. The concise form of this equation can also be written as follows.

$$
p_w^h(\mathbf{x}, t) = \begin{bmatrix} \mathbf{N}_w(\mathbf{x}) & \mathbf{N}_w^{\text{enr}}(\mathbf{x}) \end{bmatrix} \cdot \begin{bmatrix} \mathbf{P}_w(t) \\ \widetilde{\mathbf{P}}_w(t) \end{bmatrix} = \overline{\mathbf{N}}_w \cdot \overline{\mathbf{P}}_w
\tag{18}
$$

where $\mathbf{N}_w^{\text{enr}}(\mathbf{x})$ can be obtained from Equation (17). The full procedure of deriving the weak forms of governing equations can be found in Mohammadnejad and Khoei (2013a, 2013b); Khoei et al., (2014, 2015, 2016a, 2016b, 2018); Khoei and Mortazavi (2020). By introducing the above-mentioned approximation functions and their corresponding test functions into the weak forms, the final set of nonlinear equations can be obtained as

$$
\mathbf{M}_{uu}\ddot{\overline{\mathbf{U}}} + \mathbf{K}_{uu}\overline{\mathbf{U}} - \mathbf{Q}_{uw}\overline{\mathbf{P}}_w + \mathbf{F}_{\ddot{u}}^{int} = \mathbf{F}_u^{\text{ext}}
\tag{19}
$$

$$
\mathbf{M}_{wu}\ddot{\overline{\mathbf{U}}} + \mathbf{Q}_{uw}^{\mathrm{T}}\dot{\overline{\mathbf{U}}} + \mathbf{C}_{ww}\dot{\overline{\mathbf{P}}}_w + \mathbf{H}_{ww}\overline{\mathbf{P}}_w - \mathbf{F}_w^{int} = \mathbf{F}_w^{\text{ext}}
\tag{20}
$$

where the definitions of the introduced matrices and vectors are given in Appendix A. The temporal discretization is performed using the generalised Newmark scheme. Furthermore, since this set of equations is nonlinear, it is linearised and solved by the Newton-Raphson method (Mohammadnejad and Khoei, 2013a, 2013b).

2.3. Computational notes

It is recalled that the basic requirements for a convergent numerical representation of a differential equation are that the approximation converges to the exact derivative relations (consistency) and that round-off and related errors do not grow during the solution process (stability). For strict definitions, refer to Richtmyer and Morton (1967); Ortega and Rheinboldt, (1970); Morris (1983). For partial differential equations of the initial value type addressed here, there is a phenomenon that has no counterpart in ordinary differential equations; in fact, successive refinement of the interval length may give an approximate solution which is stable but may converge to the solution of a different differential equation (is inconsistent). A well-known example for this is the Du Fort-Frankel scheme for a linear parabolic equation with finite differences in space and time (Allen et al., 1988). It can also occur for finite elements in space and Finite Differences in time; see, for example, Farhat and Sobh, (1990); Turska and Schrefler (1993). It seems that another example is the case of fracturing of saturated porous media, governed by the Biot equations and a cohesive fracture model. A numerical solution of this problem requires the approximation of the governing equation and a fracture tip advancement/time-step algorithm. Monolithic numerical solutions of the Biot equations usually satisfy the consistency condition. However, when modelling fracture advancement with a cohesive model, the fracture tip advancement/time-step algorithm, if not properly chosen, introduces a constraint for the velocities at play. These velocities are the advancement velocity of the crack tip and that of the fluid in the fracture and in the surrounding region of the crack tip. Hence, the discretised Biot equations plus a constraint on the velocities may give upon successive refinement of the interval length an approximate solution which is stable but may converge to the solution of a different differential equation (is inconsistent).

From this reasoning it appears that the following necessary condition

for the fracture tip advancement/time-step algorithm to obtain a consistent solution, if activated, is the following.

$$
\forall t \quad Ds = m \, ds \quad (m \geqslant 1)
\tag{21}
$$

where t is the time step, ds is the algorithmic crack tip advancement, and Ds is the resulting crack advancement within the time step; $m = 1$ with constant t means the constant velocity of advancement per step. Equation (21) implies that the algorithm should not impose an upper limit of the crack tip advancement velocity, which means that several algorithmic crack tip advancements ds are possible within a time step. In such a way, the interference of the algorithm with the velocities at play is as small as possible. Equation (21) also satisfies the requirement of respecting the self-organisation of the rupture needed to obtain physically meaningful results (Peruzzo et al., 2019a).

The crack growth algorithm in this study works in the following way; at the end of each step after convergence, the maximum tensile stress is checked over all sampling points of the element that neighbours the current tip element. If the maximum tensile stress violates the cohesive strength at all sampling points, the state of the element changes from intact to cohesive, which means that the fracture must propagate through it. Then, the next candidate element for propagation is also checked. This procedure continues for all elements that are plausible for fracturing. Sometimes, it may be necessary to let enucleate multiple fractures in an HF problem, as, for instance, in fracture forerunning. This is the case where ahead of a mother crack, one or more daughter cracks appear which in time coalesce causing a jump in the tip advancement and resulting in an apparent velocity of the main crack which can be larger than that of the P wave. (Slepyan et al., 2015; Ni et al., 2021). Therefore, the fracture is allowed to cross as many elements as meets this criterion. We recall that the focus of this study was on the irregular and stepwise propagation of fracture under the simplest problem specifications, namely symmetric problems with a linear material and a linear cohesive model. Heterogeneity and fracture branching were ignored, which could already cause irregularity and prevent any useful discussions. In other words, the aim is to present the irregular and stepwise behaviour when they are less expected. With respect to these assumptions, the fracturing algorithm was applied only to the elements on the axis of symmetry. The contact algorithm was also implemented in the examples presented since the HF can result in fluid delay for low permeable rocks, as demonstrated by Mohammadnejad and Khoei (2013b). This fluid lag can result in fracture closure when the fluid suction is considerable and the loading is not monotonous, as is the case with dynamic problems.

3. Numerical results of case studies

3.1. Hydraulic fracturing in an infinite medium

In the first example, we review the original problem solved by Mohammadnejad and Khoei (2013a) in Section 6.2, which is marked by "C0" here. It is a dynamic hydraulic fracturing problem in an infinite medium with an injection rate of $Q = 0.0001 \text{ m}^2/\text{s}$ without initial perforation. On the virtue of symmetry, one-half of the domain is modelled. A fixed time step of $\Delta t = 0.01$ s is assumed. The geometry and specifications of the problem are given in Fig. 2 and Table 1, respectively.

Fig. 3 presents the results of the C0 model on both the linear scale and log–log scale. The log–log scale graphs illustrate that while the results seem to be smooth and regular at the later times, it is not the case at the beginning, particularly it can be observed more clearly from the Crack Mouth Pressure (CMP) and Crack Mouth Opening Displacement (CMOD) curves. Furthermore, the graphs illustrate almost linear trends on the log–log scale. This is especially in accordance with the algebraic expressions of the KGD model that are in power relationships with time, as given below.
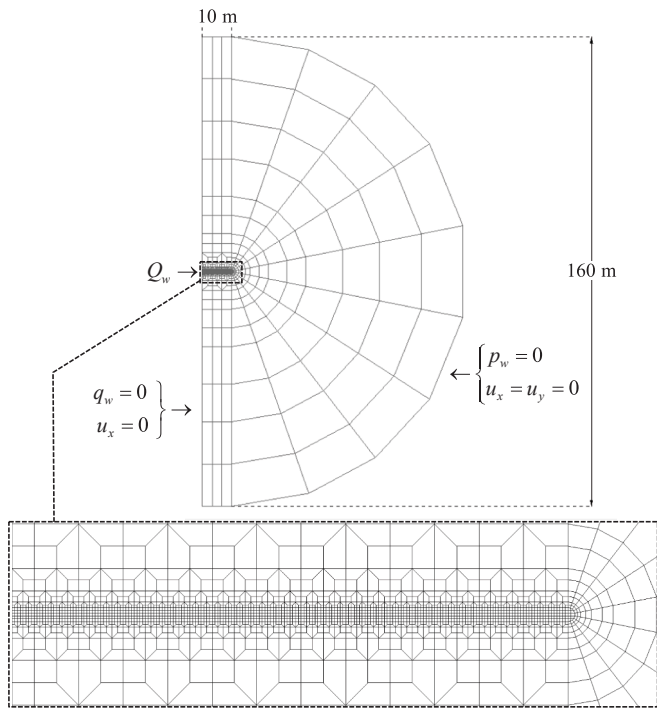
Fig. 2. The geometry, boundary conditions and finite element mesh of hydraulic fracturing problem in an infinite medium.

Table 1
Material properties of HF problem in an infinite medium.

Material property	Symbol	Value	Unit
Elasticity modulus	E	15.96	GPa
Poisson ratio	ν	0.2	–
Porosity	n	0.19	–
Biot coefficient	α	0.79	–
Bulk modulus of solid	K_s	36.0	GPa
Intrinsic permeability	k	6.0×10^{-15}	m^2
Dynamic viscosity	μ_w	10^{-3}	Pa s
Solid density	ρ_s	2000.0	$\frac{kg}{m^3}$
Fluid density	ρ_w	1000.0	$\frac{kg}{m^3}$
Cohesive strength	σ_c	0.45	MPa
Cohesive fracture energy	G_c	143.0	$\frac{N}{m}$

$$\text{CMOD} = 1.87\left(\frac{\mu_w(1-\nu)Q^3}{G}\right)^{1/6} t^{1/3}$$

$$\text{CL} = 0.68\left(\frac{GQ^3}{\mu_w(1-\nu)}\right)^{1/6} t^{2/3} \tag{22}$$

$$\text{CMP} = 1.135\left(\frac{G^3 Q \mu_w}{(1-\nu)^3 L^2}\right)^{1/4} + S$$

where G is the shear modulus, L is the crack length and S is the in-situ stress normal to the crack growth direction. However, evaluation on the crack length (CL) slope of the Crack Length (CL) in the log–log scale reveals that this slope is not equal exactly to that of the KGD solution. It is about 0.60 in the current simulation, while 0.6667 from the KGD relations. The difference can be more significant in other problems as later demonstrated, and it depends on the problem specifications; i.e. how far they are from the simplified conditions of the analytical solution.

Fig. 4 presents the results of the same example under quasi-static (Q-Stat) conditions compared to the original dynamic (Dyn) solution.

Obviously, almost no difference can be observed between the two cases. It means that the dynamic effects are negligible in this example. As it can be seen later, the quasistatic solutions obtained with the present model for different problems are often regular; hence, the regular and smooth crack growth observed by Mohammadnejad and Khoei (2013a) can be attributed to negligibility of the dynamic effects. Nevertheless, the log–log scale plots at the bottom of the quasi-static figure show that the results are smoother at the beginning comparing to the results of dynamic solution results in Fig. 3, which means that small dynamic effects are obvious at the beginning, but they vanish quickly. A crucial point to be noted in the KGD relations is that these relations are independent of any strength properties of the medium, as they are derived for the viscosity-dominated regime of HF in which the influence of fracture toughness is negligible in the balance equations (Geertsma and Haafkens, 1979). It means that they work only for some special cases of the HF problems. On the contrary, we have observed that the cohesive strength directly controls the propagation velocity and dynamic effects. This observation is also in agreement with some more complicated closed-form solutions, for instance the ones proposed by Detournay, (2016), in which the toughness is not disregarded. It means that the cohesive strength must always be tuned for the purpose of validation with the KGD relations. It should be noted that we tried to increase the dynamic effects in this example by increasing the injection rate and decreasing the viscosity, however, the results remained almost smooth and regular. The reason may be related to the value of cohesive strength, which controls the propagation velocity and prevents further dynamic effects. It can also justify the smooth and regular results reported by other researchers, such as Kresse et al. (2011); Fathima and de Borst, (2019); Jafari et al., (2021), where their problem definitions were not dynamic, or their cohesive strength values could be relatively high.

The problem is now modified to highlight the dynamic effects. In this case, which is designated as the "C1" model, all specifications are the same as the "C0" model, except that the intrinsic permeability, the injection rate, and the time step size are, respectively, multiplied by 1000, 2000, and 0.001. Additionally, the cohesive strength and fracture energy are replaced by 0.02 MPa and 12.712 N/m, respectively. These parameters are chosen to obtain more representative results. The results are shown in Fig. 5; it can be clearly observed that the growth is irregular and the growth length per step (or the propagation velocity) is not constant at different time steps. Furthermore, a jump occurs in the propagation of the fracture at about 0.96 ms, which is a sign of the stepwise behaviour. To better distinguish the curves of CL in Fig. 5(a), the damage index of the elements is plotted along the fracture path in Fig. 6. In this figure, damage indices 0 and 1 display the intact and fractured status, respectively. Fig. 6 illustrates that in a dynamic fracturing problem it is possible for multiple instances of fracture to occur at the same time, which is called 'fracture forerunning'. To preserve comprehensibility, the position of only two of the fracture tips, as well as the total length of the damaged segments, are demonstrated in Fig. 5(a). The tips are marked by the 'First tip' and the "Last tip", as shown in Fig. 6. These two tips usually coincide, especially under low dynamic conditions; however, they are distinguishable when a fracture forerunning occurs. The jumps originate from sudden fracturing of the intact segments in between the forerunning segments and the main (mother) crack. Thus, fracture forerunning is one of the main reasons of the stepwise behavior. The CMP and CMOD plotted in Fig. 5(b) and (c), still present the power relationship with the time similar to the case C0; however, the CMP is a little oscillatory due to dynamic effects and irregular extensions of the fracture length.

In Fig. 7, a comparison is made between the quasi-static and dynamic solutions of the C1 model. This figure reveals that the irregular and stepwise behaviour of C1 in Fig. 5 was correctly attributed to the dynamic effects, since the quasi-static solutions show smooth power relationships with time in CL, CMP, and CMOD. Fig. 7(a) illustrates that the dynamic growth is slower at first, but it eventually takes over the quasi-static crack length. The results of CMP and CMOD for the two
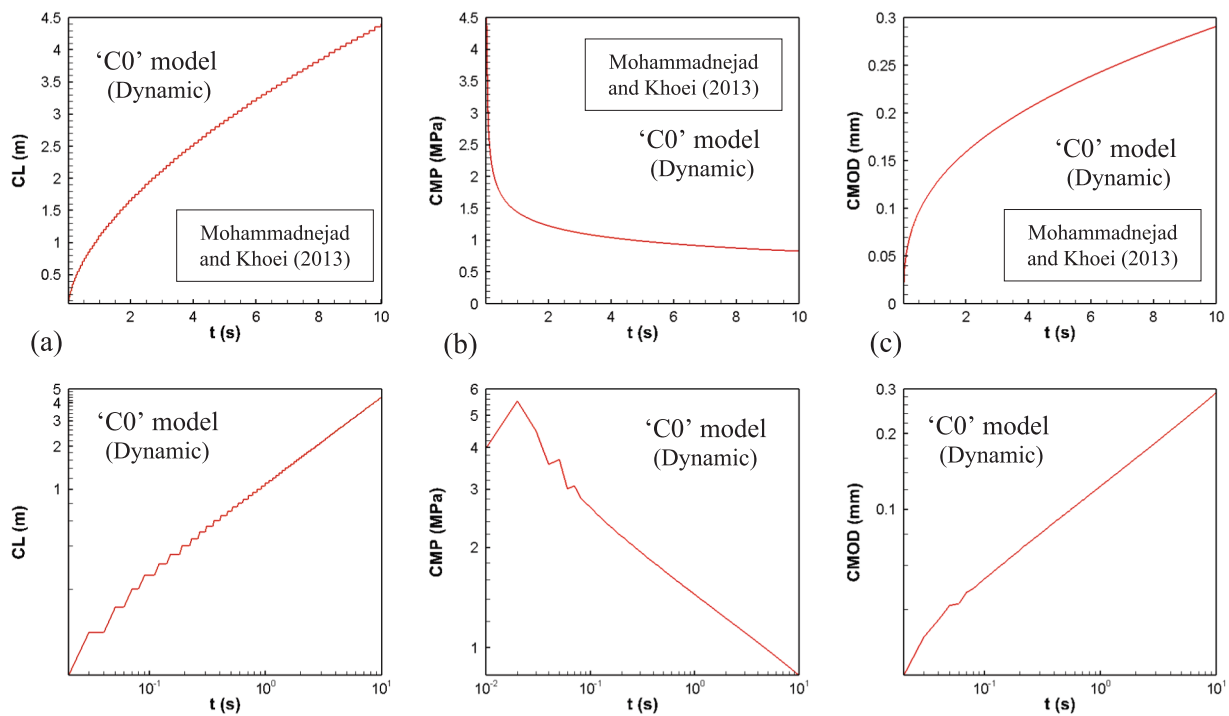
Fig. 3. The time histories of (a) Crack Length (CL), (b) Crack Mouth Pressure (CMP), and (c) Crack Mouth Opening Displacement (CMOD) for the case study "C0"; The results of **Mohammadnejad and** Khoei **(2013)** in the linear scale (top) and log–log scale (bottom).
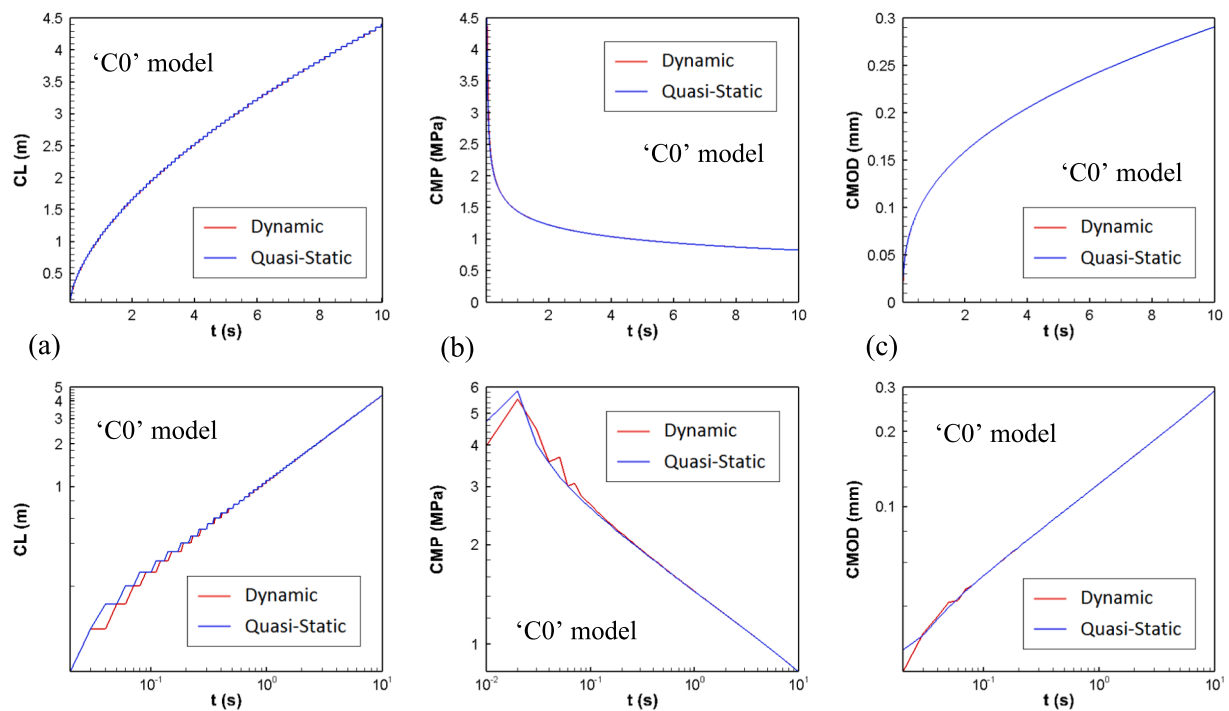

Fig. 4. The time histories of (a) CL, (b) CMP, and (c) CMOD for the case study "C0"; A comparison between the Quasi-Static (Q-Stat) and Dynamic (Dyn) solutions in the linear scale (top) and log–log scale (bottom).

cases are close to each other, as shown in Fig. 7. These investigations highlight that the dynamic effects become significant when the injection rate is high or the fluid viscosity is low, i.e. the Reynolds number is high. It is also in accordance with the experimental observations reported by Lhomme et al. (2002). Nevertheless, the viscosity could amplify the dynamic behaviour only when it decreases far from its realistic range. It

should also be noted that the proposed model is based on the laminar flow assumption within the fracture, and it is not eligible to be used for very high Reynolds numbers where the flow is turbulent. However, Vahab and Khalili, (2017) concluded for the case studies conducted using a similar approach for the HF problem with the same geometry as C0 and C1 that the fluid pressure curves obtained from the laminar and
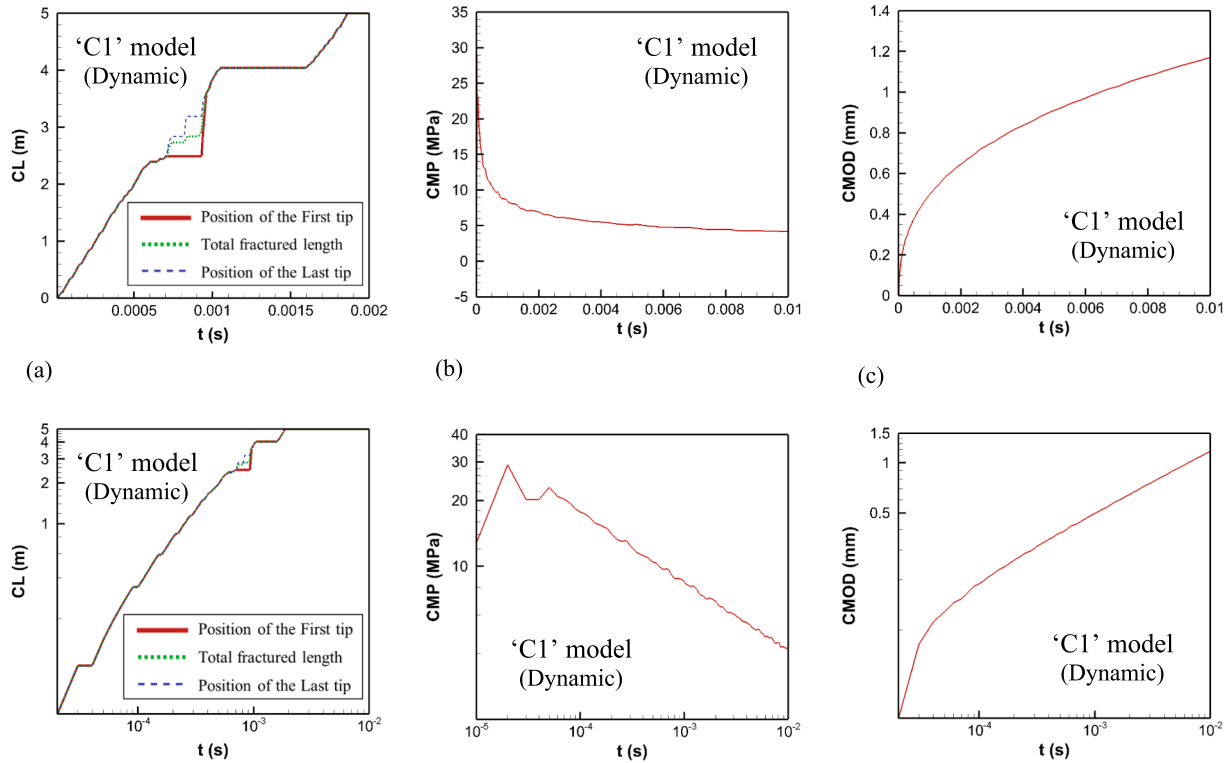
Fig. 5. Time histories of (a) CL, (b) CMP, and (c) CMOD for the case study "C1"; the Dynamic (Dyn) solution in the linear scale (top) and log–log scale (bottom) – the "First tip" and "Last tip" in Fig. 5(a) are defined in Fig. 6.
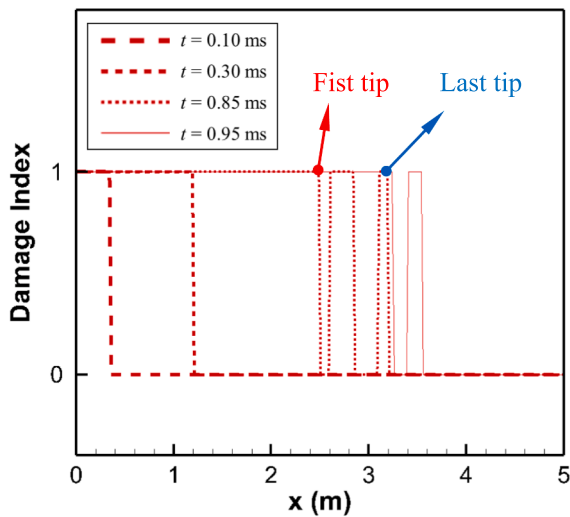

Fig. 6. Damage index of the elements along the fracture path at differnet times for the case study "C1" (Dynamic model); The damage indices 0 and 1 show the intact and fractured status, respectively – The "First tip" and the "Last tip" are demonstrated for $t = 0.85$ ms.

turbulent flow formulations are close for the Reynolds numbers of 2×10^4. In this regard, case studies with high injection rates may be subjected to approximation in this article; however, the development of the presented model with turbulent flow formulation should be topic of a future study to get more accurate results. The low frequency assumption should also be revised in future studies to check its impact on the accuracy. Finally, the time histories of CL, CMP, and CMOD are plotted in Fig. 8 for the case study C1 (dynamic) at different injection rates. As

expected, the results gradually become smooth and regular as the injection rate decreases. Case studies with the injection rates of 0.2 and 0.1 m^2/s present the forerunning; therefore, they are irregular and stepwise. On the other hand, it is also interesting that the case study with $Q = 0.02$ m^2/s presents stepwise behaviour, whereas it does not undergo forerunning. Therefore, the stepwise behaviour is not necessarily a consequence of the forerunning of the fracture.

3.2. Hydraulic Fracturing of a rock plate with a fixed injection rate

In the next example, an investigation is performed for hydraulic fracturing of the 2×0.2 m^2 rock plate with a fixed injection rate. The domain was intact originally and is insulated at all boundaries except the injection point, and the displacement is fixed at the right edge, as shown in Fig. 9(a). The material properties are similar to those given in Table 1, except for the intrinsic permeability, cohesive strength, and cohesive fracture energy, which are respectively modified as $k = 6 \times 10^{-19}$ m^2, $\sigma_c = 0.1$ MPa, and $G_c = 95$ N/m. The fluid is injected at the rate of $Q = 0.2$ m^2/s. This base case is marked "C10" hereafter. Since spatial and temporal discretizations can be substantially influential on the results of a dynamic problem, the results of C10 (dynamic model) with different time step and horizontal discretization sizes are presented in Fig. 10. An unstructured mesh was also used, which is depicted in Fig. 9(b). It should be noted that all the results are obtained assuming the first fifty steps with constant $\Delta t = 10^{-7} s$ because of the criticality of the fracture initiation in the early stages. The results of different discretizations are reasonably close, as can be seen in Fig. 10, especially for CMP and CMOD. Moreover, the results illustrate that the forerunning and the stepwise growth are considerably more distinct than C1 (dynamic model), described in the previous section. The reason is geometry and boundary conditions, where the closer boundaries to the fracturing region in the C10 model can reflect the induced waves, and the wave interference is recurrent. As can be seen in Fig. 10 (a), results of CL are
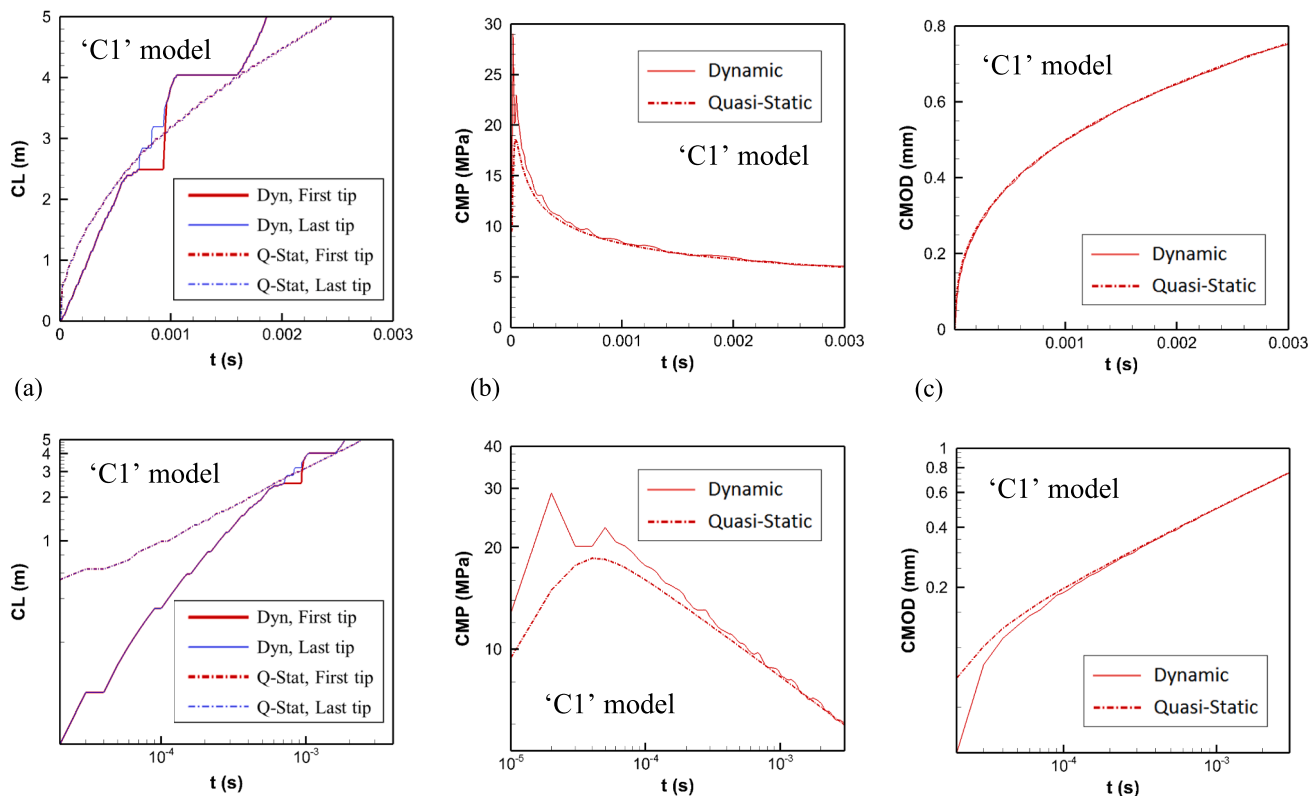
Fig. 7. Time histories of (a) CL, (b) CMP, and (c) CMOD for the case study "C1"; A comparison between the Quasi-Static (Q-Stat) and Dynamic (Dyn) solutions in the linear scale (top) and log–log scale (bottom).
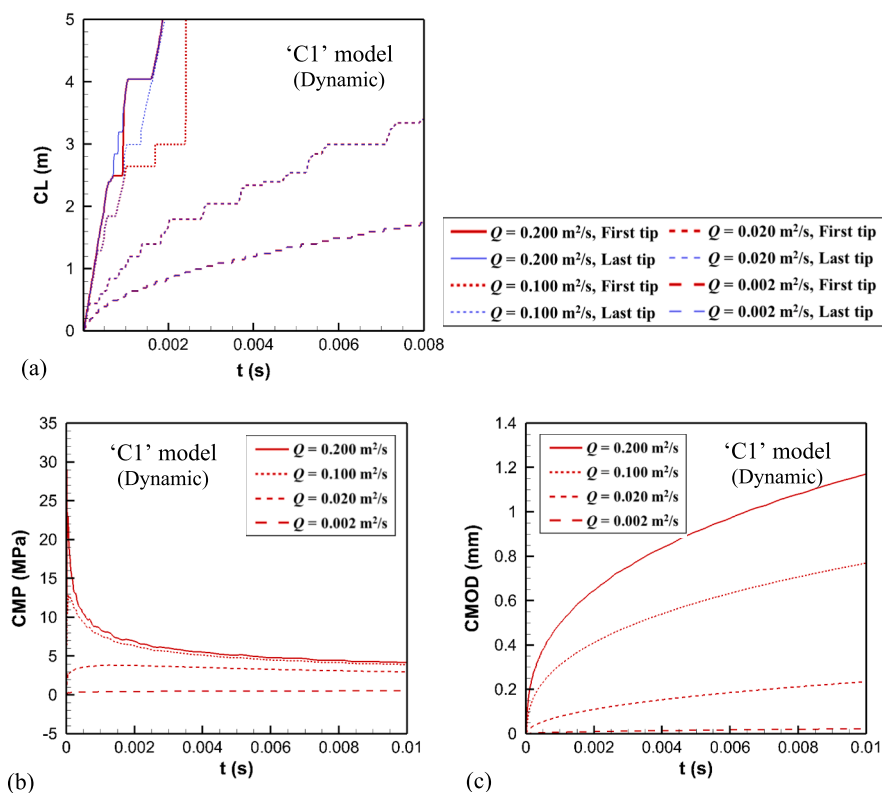

Fig. 8. Time histories of (a) CL, (b) CMP, and (c) CMOD for the case study "C1" (Dynamic) at different injection rates.
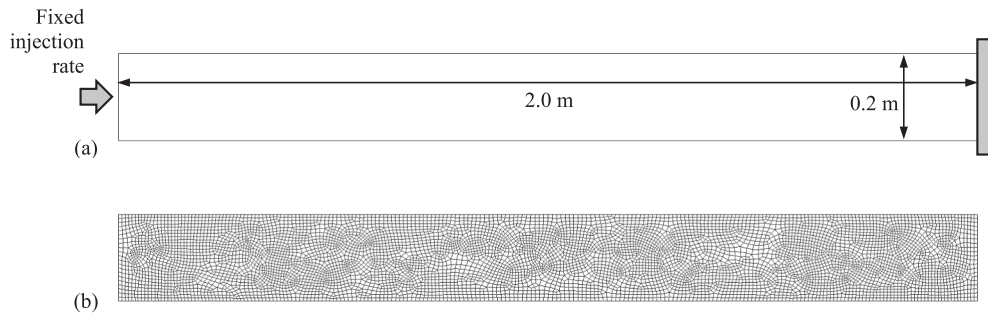
Fig. 9. Hydraulic fracturing for a plate with a fixed injection rate; (a) geometry and boundary conditions, (b) an unstructured mesh proposed for the mesh-independency assessment of the model.
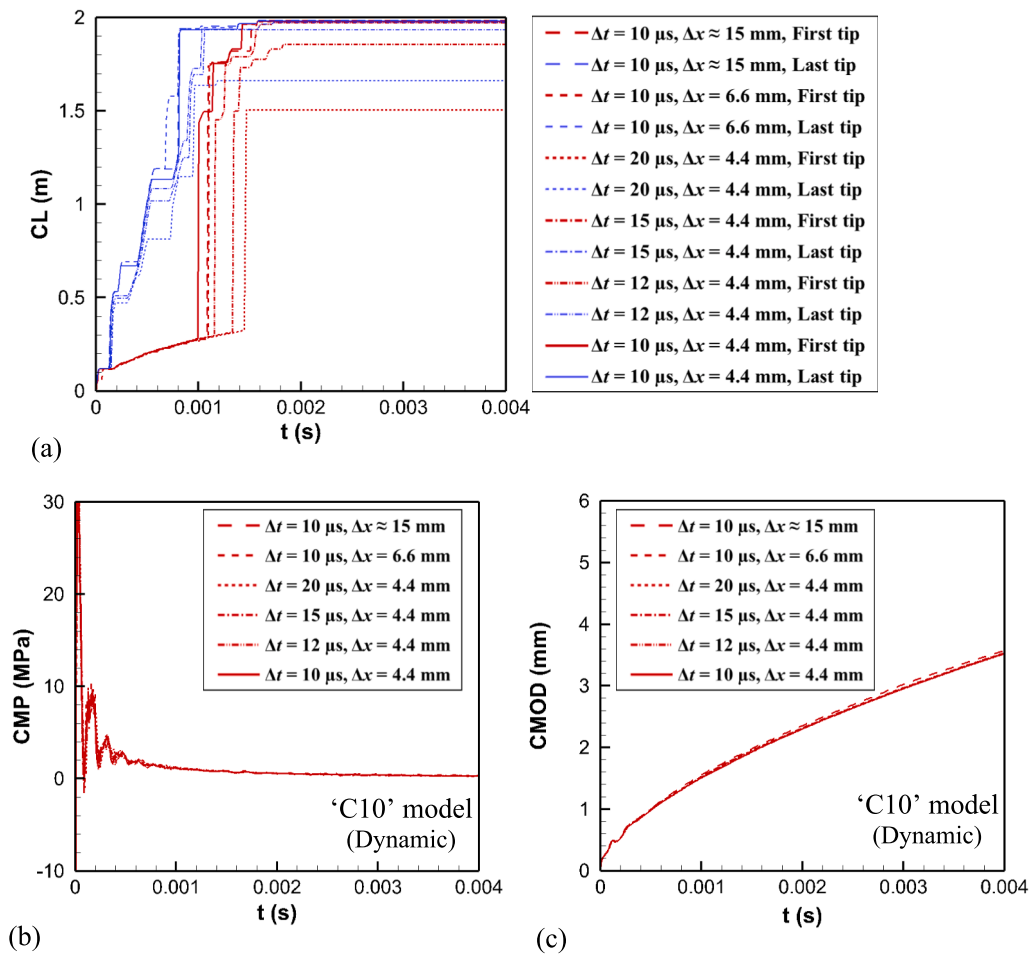

Fig. 10. Time histories of (a) CL, (b) CMP, and (c) CMOD for the case study "C10" (Dynamic model) at different spatial and temporal discretization – The case study with $\Delta x \approx 15$mm refers to the unstructured mesh.

more sensitive to the time step rather than the spatial discretization that can be attributed to the relative size of the time step and the period of stress waves in the vicinity of the fracture tip. When the fracture propagates, the tip crosses over all elements violating the cohesive strength to reach the first element with close but lower tensile stress than the cohesive strength. In such a case, there are mainly two states for the stress at the current tip element; i.e. the tensile stress can be either ascending or descending, according to the wave propagation. If the time step is not fine enough, the tip stress variation can pass over the ascending or descending phase and enter the opposite phase. This can play a key role in the propagation scenario because the tip stress fluctuations are usually close to the cohesive strength of the medium, since

the tip of the fracture passes through the elements that have just violated the cohesive strength. Therefore, it can be concluded that the time step size is especially crucial for accurate fracture growth modelling in dynamic problems. Considering $\Delta x = 4.4$mm and $\Delta t = 10^{-2}$ ms as reference discretization, a comparison is performed in Fig. 11 between dynamic and quasi-static solutions for the C10 model. As expected, the quasi-static solution for CL, CMP, and CMOD led to smooth and regular results. The difference between the results of the dynamic and quasi-static cases is significant; however, it is interesting that the "first tip" curve in the dynamic case is close to the quasi-static solution for a while. It was not the case for the C1 model in Fig. 7, though.

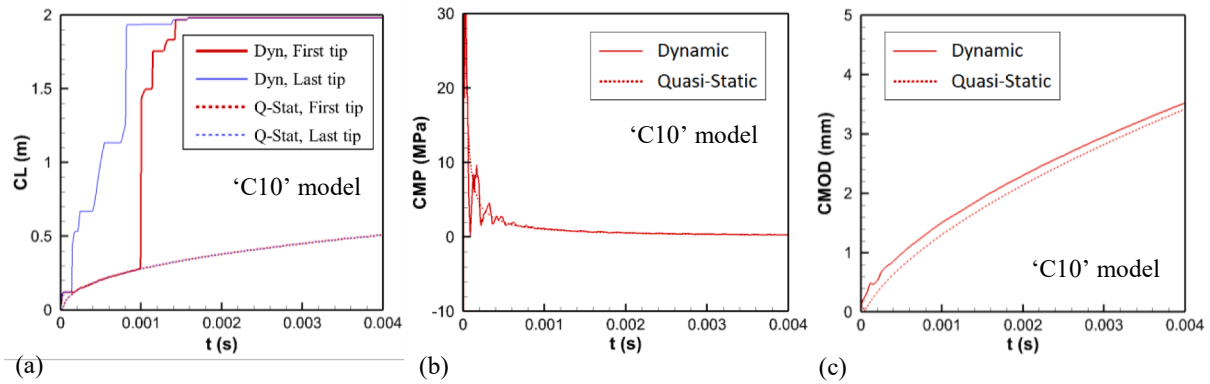The effect of injection rate is also investigated for the C10 model, as

Fig. 11. Time histories of (a) CL, (b) CMP, and (c) CMOD for the case study "C10"; A comparison between the Quasi-Static (Q-Stat) and Dynamic (Dyn) solutions.

shown in Fig. 12. Similarly to the conclusion made for the C1 model in Fig. 8, the irregular and stepwise behaviour gradually vanishes as the injection rate decreases. Furthermore, the C10 model is solved assuming different values of the elastic modulus, fluid viscosity, and intrinsic permeability. Fig. 13(a) illustrates that reducing the elastic modulus decreases the propagation speed as well as the dynamic irregularities. It can be justified by the fact that the permeability of the C10 model is very low; therefore, the fixed volume injection rate results in an almost displacement-controlled loading on the solid. It means that the lower elastic modulus results in less induced tensile stress at the fracture tip and consequently slower fracture propagation. Furthermore, the viscosity influence shown in Fig. 13(b) illustrates that the practical values of the water viscosity could not change the growth considerably; nonetheless, this figure shows that higher viscosities can delay the jump of the First tip to join the last tip. Finally, Fig. 13(c) reveals that increasing matrix permeability increases the growth speed in this particular problem; even though lower permeability results in higher fracture propagation speeds due to less fluid loss into the matrix. However, it is crucial to note that the problem setup in the C10 model can bring about considerable levels of fluid lag, as depicted in Fig. 14. This figure presents the distribution of the normal effective stress only in intact elements along the symmetry axis. When comparing Fig. 14(a) and 14(b), it can be seen that $k = 6 \times 10^{-15}$ m² results in a lagged propagation, while this is not the case for $k = 6 \times 10^{-11}$ m². This means that the violation of the cohesive strength takes place easier in the case

that does not encounter the fluid lag; hence, the growth rate is higher there. It is also interesting that the results of $k = 6 \times 10^{-15}$ m² and $k = 6 \times 10^{-19}$ m² do not differ considerably in Fig. 13(c), which means that $k = 6 \times 10^{-15}$ m² can already imply impermeability of the rock for this example.

4. Conclusions

In the present study, several parametric analyses were presented to examine the stepwise and irregular behaviour of hydraulic fracturing using the XFEM with a linear cohesive crack model and the maximum tensile stress criterion for fracture propagation. The porous domain was assumed to be permeable, homogeneous, and saturated. Two sets of examples were simulated, including the hydraulic fracturing of an infinite medium and the hydraulic fracturing of a rock plate with a fixed injection rate. The injection rate, elastic modulus, fluid viscosity, intrinsic permeability, mesh size, and time step size were the variables of the parametric analyses. It was shown that the prerequisite for the regularity of fracture propagation is the negligibility of dynamic effects. Therefore, if the advancement algorithm is consistent in a dynamic numerical model and still yields smooth and regular results, it can be justified by the problem specifications that do not bring about high dynamics. It was shown that under quasistatic conditions, the obtained results of CMP, CMOD, and CL for the infinite medium were smooth and regular and followed power trends. Similarly, the quasi-static case
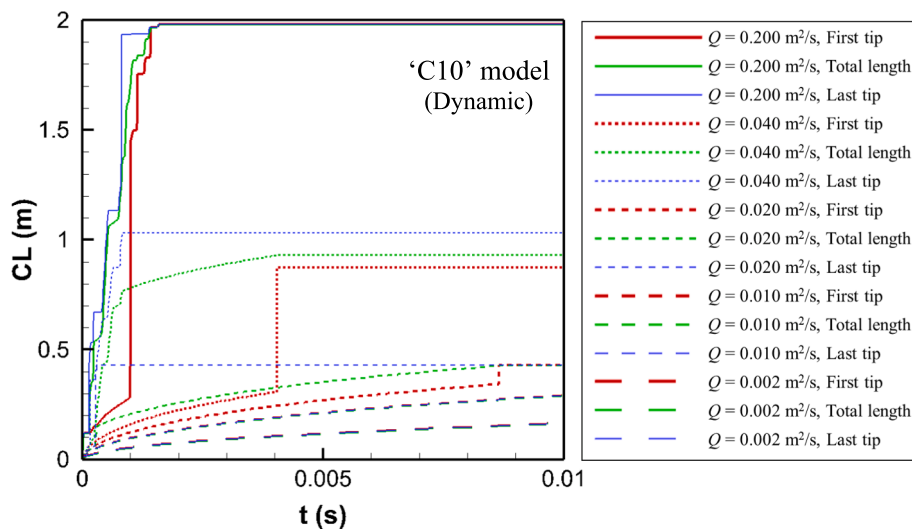

Fig. 12. Time history of CL for the case study "C10" (Dynamic model) at different injection rates.
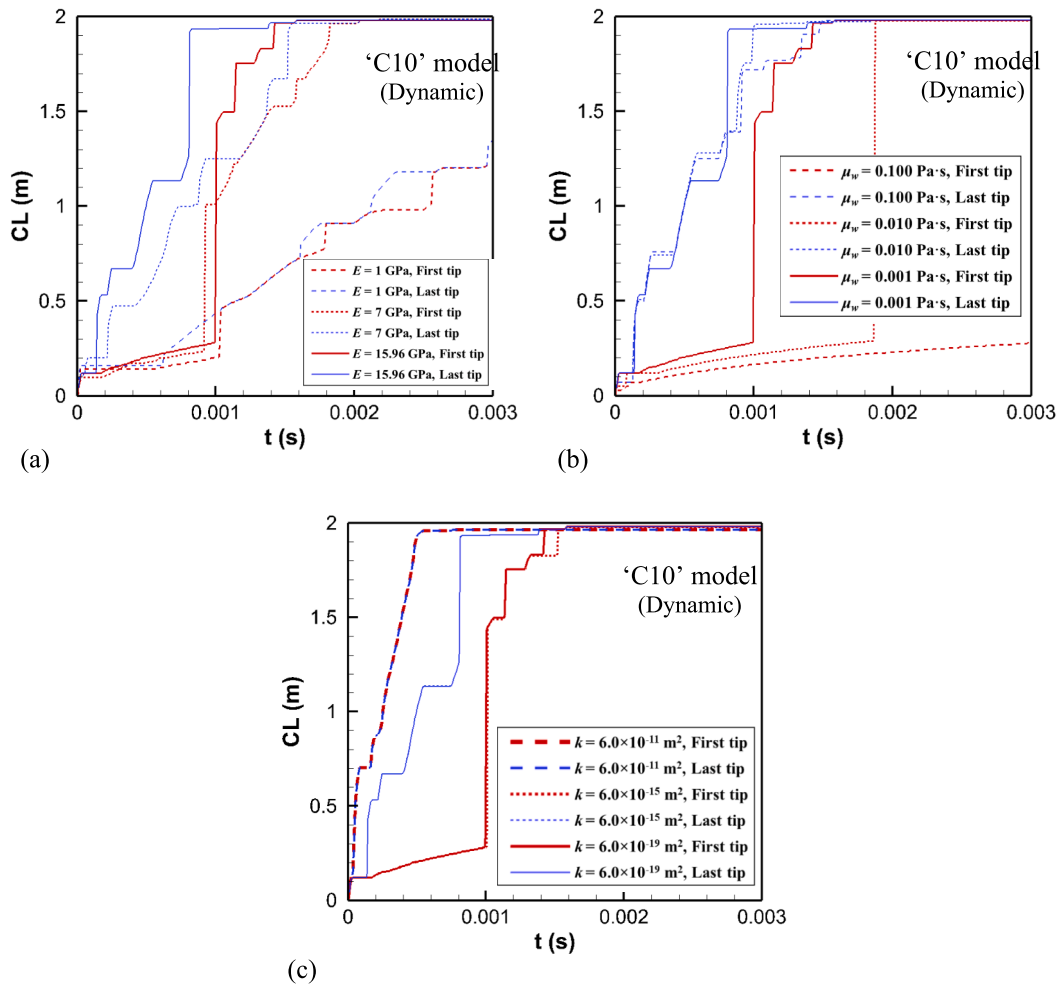
Fig. 13. Time histories of CL for the case study "C10" (Dynamic model) for different values of (a) elastic modulus, (b) fluid viscosity, and (c) intrinsic permeability.
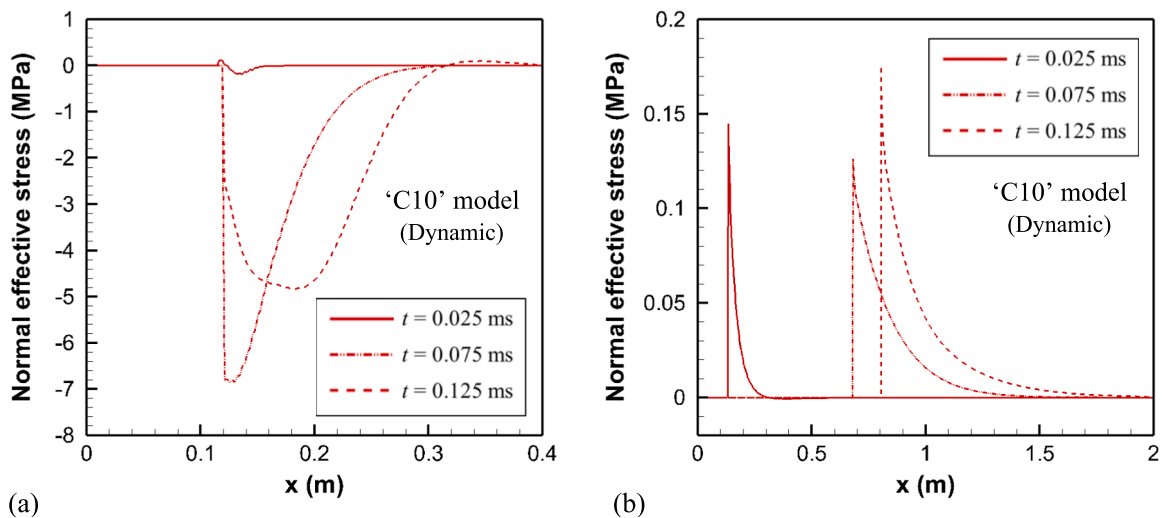
Fig. 14. Distributions of normal effective stress in the intact elements along the axis of symmetry for the case study "C10" (Dynamic model) using (a) $k = 6 \times 10^{-15}$ m^2 and (b) $k = 6 \times 10^{-11}$ m^2 at different times.

studies on the rock plate also presented power trends; however, the boundary conditions of displacement for the rock plate could sometimes affect these trends due to finite dimensions of the medium. In contrast to quasi-static conditions, the results of dynamic problems were often irregular. It can be attributed to wave propagation and stress fluctuation at the tip of the fracture, as discussed above. It was concluded that

forerunning of the fracture can bring about further irregular and step-wise growth, as also mentioned by Ni et al. (2021). Dynamic effects can hinder the propagation of the main tip for a short time and then cause a sudden crack growth that emits stronger waves. Accordingly, cracks advance faster overall in dynamic cases compared to quasistatic ones. Evidently, these observations could be achieved by means of a consistent algorithm for fracture growth that does not limit the growth length per step. Our investigations illustrate that the dynamic effects get significant for higher Reynolds numbers. It is also in accordance with the experimental observations reported by Lhomme et al. (2002). This means that both smooth and stepwise results as well as regular and irregular results reported in the literature can be credible, and it all comes down to the problem specifications and material properties. Finally, it should be recalled that the current model is established based on the low-frequency assumption that neglects the fluid inertia. While being a prevalent assumption, it is not precise enough for some extreme cases of dynamic problems. In addition, the turbulence in high Reynolds numbers can violate the laminar flow assumption employed in this study and result in the lack of accuracy. However, the focus of this study was on the irregular and stepwise propagation of fracture under the simplest problem specifications, namely symmetric problems with a linear material and a linear cohesive model. Furthermore, heterogeneity and fracture branching were also neglected, because they could already bring about irregularity and prevent any useful discussion. In other words, showing the irregular and stepwise behavior when they are less expected was the purpose. After all, the impact of these factors should be addressed in future studies.

Declaration of Competing Interest

The authors declare that they have no known competing financial interests or personal relationships that could have appeared to influence the work reported in this paper.

Data availability

No data was used for the research described in the article.

Appendix A. .

The coefficient matrices of the discretized equations (19) and (20) are presented here. The matrices can be obtained as

$$\mathbf{K}_{uu} = \begin{bmatrix} \int_{\Omega} \mathbf{B}^{\mathrm{T}}\mathbf{D}\mathbf{B}\,\mathrm{d}\Omega & \int_{\Omega^{\mathrm{enr}}} \mathbf{B}^{\mathrm{T}}\mathbf{D}\mathbf{B}^{\mathrm{enr}}\,\mathrm{d}\Omega \\ \int_{\Omega^{\mathrm{enr}}} (\mathbf{B}^{\mathrm{enr}})^{\mathrm{T}}\mathbf{D}\mathbf{B}\,\mathrm{d}\Omega & \int_{\Omega^{\mathrm{enr}}} (\mathbf{B}^{\mathrm{enr}})^{\mathrm{T}}\mathbf{D}\mathbf{B}^{\mathrm{enr}}\,\mathrm{d}\Omega \end{bmatrix} \tag{A.1}$$

$$\mathbf{M}_{uu} = \begin{bmatrix} \int_{\Omega} \mathbf{N}_u^{\mathrm{T}}\rho\mathbf{N}_u\,\mathrm{d}\Omega & \int_{\Omega^{\mathrm{enr}}} \mathbf{N}_u^{\mathrm{T}}\rho\mathbf{N}_u^{\mathrm{enr}}\,\mathrm{d}\Omega \\ \int_{\Omega^{\mathrm{enr}}} (\mathbf{N}_u^{\mathrm{enr}})^{\mathrm{T}}\rho\mathbf{N}_u\,\mathrm{d}\Omega & \int_{\Omega^{\mathrm{enr}}} (\mathbf{N}_u^{\mathrm{enr}})^{\mathrm{T}}\rho\mathbf{N}_u^{\mathrm{enr}}\,\mathrm{d}\Omega \end{bmatrix} \tag{A.2}$$

$$\mathbf{M}_{wu} = \begin{bmatrix} \int_{\Omega} \nabla\mathbf{N}_w^{\mathrm{T}}(k_w\rho_w)\mathbf{N}_u\,\mathrm{d}\Omega & \int_{\Omega^{\mathrm{enr}}} \nabla\mathbf{N}_w^{\mathrm{T}}(k_w\rho_w)\mathbf{N}_u^{\mathrm{enr}}\,\mathrm{d}\Omega \\ \int_{\Omega^{\mathrm{enr}}} (\nabla\mathbf{N}_w^{\mathrm{enr}})^{\mathrm{T}}(k_w\rho_w)\mathbf{N}_u\,\mathrm{d}\Omega & \int_{\Omega^{\mathrm{enr}}} (\nabla\mathbf{N}_w^{\mathrm{enr}})^{\mathrm{T}}(k_w\rho_w)\mathbf{N}_u^{\mathrm{enr}}\,\mathrm{d}\Omega \end{bmatrix} \tag{A.3}$$

$$\mathbf{Q}_{uw} = \begin{bmatrix} \int_{\Omega} \mathbf{B}^{\mathrm{T}}\alpha\mathbf{m}\mathbf{N}_w\,\mathrm{d}\Omega & \int_{\Omega^{\mathrm{enr}}} \mathbf{B}^{\mathrm{T}}\alpha\mathbf{m}\mathbf{N}_w^{\mathrm{enr}}\,\mathrm{d}\Omega \\ \int_{\Omega^{\mathrm{enr}}} (\mathbf{B}^{\mathrm{enr}})^{\mathrm{T}}\alpha\mathbf{m}\mathbf{N}_w\,\mathrm{d}\Omega & \int_{\Omega^{\mathrm{enr}}} (\mathbf{B}^{\mathrm{enr}})^{\mathrm{T}}\alpha\mathbf{m}\mathbf{N}_w^{\mathrm{enr}}\,\mathrm{d}\Omega \end{bmatrix} \tag{A.4}$$

$$\mathbf{C}_{ww} = \begin{bmatrix} \int_{\Omega} \mathbf{N}_w^{\mathrm{T}}\left(\frac{\alpha-n}{K_s}+\frac{n}{K_w}\right)\mathbf{N}_w\,\mathrm{d}\Omega & \int_{\Omega^{\mathrm{enr}}} \mathbf{N}_w^{\mathrm{T}}\left(\frac{\alpha-n}{K_s}+\frac{n}{K_w}\right)\mathbf{N}_w^{\mathrm{enr}}\,\mathrm{d}\Omega \\ \int_{\Omega^{\mathrm{enr}}} (\mathbf{N}_w^{\mathrm{enr}})^{\mathrm{T}}\left(\frac{\alpha-n}{K_s}+\frac{n}{K_w}\right)\mathbf{N}_w\,\mathrm{d}\Omega & \int_{\Omega^{\mathrm{enr}}} (\mathbf{N}_w^{\mathrm{enr}})^{\mathrm{T}}\left(\frac{\alpha-n}{K_s}+\frac{n}{K_w}\right)\mathbf{N}_w^{\mathrm{enr}}\,\mathrm{d}\Omega \end{bmatrix} \tag{A.5}$$

$$\mathbf{H}_{ww} = \begin{bmatrix} \int_{\Omega} \nabla\mathbf{N}_w^{\mathrm{T}}(k_w)\nabla\mathbf{N}_w\,\mathrm{d}\Omega & \int_{\Omega^{\mathrm{enr}}} \nabla\mathbf{N}_w^{\mathrm{T}}(k_w)\nabla\mathbf{N}_w^{\mathrm{enr}}\,\mathrm{d}\Omega \\ \int_{\Omega^{\mathrm{enr}}} (\nabla\mathbf{N}_w^{\mathrm{enr}})^{\mathrm{T}}(k_w)\nabla\mathbf{N}_w\,\mathrm{d}\Omega & \int_{\Omega^{\mathrm{enr}}} (\nabla\mathbf{N}_w^{\mathrm{enr}})^{\mathrm{T}}(k_w)\nabla\mathbf{N}_w^{\mathrm{enr}}\,\mathrm{d}\Omega \end{bmatrix} \tag{A.6}$$

$$\mathbf{F}_u^{\mathrm{ext}} = \begin{bmatrix} \int_{\Omega} \mathbf{N}_u^{\mathrm{T}}\rho\mathbf{b}\,\mathrm{d}\Omega + \int_{\Gamma_t} \mathbf{N}_u^{\mathrm{T}}\bar{\mathbf{t}}\,\mathrm{d}\Gamma \\ \int_{\Omega^{\mathrm{enr}}} (\mathbf{N}_u^{\mathrm{enr}})^{\mathrm{T}}\rho\mathbf{b}\,\mathrm{d}\Omega + \int_{\Gamma_t^{\mathrm{enr}}} (\mathbf{N}_u^{\mathrm{enr}})^{\mathrm{T}}\bar{\mathbf{t}}\,\mathrm{d}\Gamma \end{bmatrix} \tag{A.7}$$

$$\mathbf{F}_w^{\mathrm{ext}} = \begin{bmatrix} \int_{\Omega} \nabla\mathbf{N}_w^{\mathrm{T}}k_w\rho_w\mathbf{b}\,\mathrm{d}\Omega - \int_{\Gamma_{q_w}} \mathbf{N}_w^{\mathrm{T}}\bar{q}_w\,\mathrm{d}\Gamma \\ \int_{\Omega^{\mathrm{enr}}} (\nabla\mathbf{N}_w^{\mathrm{enr}})^{\mathrm{T}}k_w\rho_w\mathbf{b}\,\mathrm{d}\Omega - \int_{\Gamma_{q_w}^{\mathrm{enr}}} (\mathbf{N}_w^{\mathrm{enr}})^{\mathrm{T}}\bar{q}_w\,\mathrm{d}\Gamma \end{bmatrix} \tag{A.8}$$

$$\mathbf{F}_u^{int} = \begin{bmatrix} \mathbf{0} \\ \int_{\Gamma_d} \mathbf{N}_u^{\mathrm{T}} \mathbf{t}_d d\Gamma - \int_{\Gamma_d} \mathbf{N}_u^{\mathrm{T}} \mathbf{n}_{\Gamma_d} p_w d\Gamma \end{bmatrix} \tag{A.9}$$

$$\mathbf{F}_w^{int} = \begin{bmatrix} -\int_{\Gamma_d} \mathbf{N}_w^{\mathrm{T}}(2h)\frac{1}{Kw}\dot{p}_w d\Gamma \\ -\int_{\Gamma_d} \mathbf{N}_w^{\mathrm{T}}(2h)\mathbf{t}_{\Gamma_d}\langle\nabla\dot{\mathbf{u}}\rangle\cdot\mathbf{t}_{\Gamma_d}d\Gamma - \int_{\Gamma_d} \mathbf{N}_w^{\mathrm{T}}[[\dot{\mathbf{u}}]]\cdot\mathbf{n}_{\Gamma_d}d\Gamma \\ -\int_{\Gamma_d} \nabla\mathbf{N}_w^{\mathrm{T}}\mathbf{t}_{\Gamma_d}(2h)(k_{wd})\nabla p_w\cdot\mathbf{t}_{\Gamma_d}d\Gamma \\ -\int_{\Gamma_d} \nabla\mathbf{N}_w^{\mathrm{T}}\mathbf{t}_{\Gamma_d}(2h)(k_{wd}\rho_w)\langle\ddot{\mathbf{u}}\rangle\cdot\mathbf{t}_{\Gamma_d}d\Gamma \\ +\int_{\Gamma_d} \nabla\mathbf{N}_w^{\mathrm{T}}\mathbf{t}_{\Gamma_d}(2h)(k_{wd}\rho_w)\mathbf{b}\cdot\mathbf{t}_{\Gamma_d}d\Gamma \\ -\int_{\Gamma_d} \left(\mathbf{N}_w^{enr}\right)^{\mathrm{T}}(2h)\frac{1}{Kw}\dot{p}_w d\Gamma \\ -\int_{\Gamma_d} \left(\mathbf{N}_w^{enr}\right)^{\mathrm{T}}(2h)\mathbf{t}_{\Gamma_d}\cdot\langle\nabla\dot{\mathbf{u}}\rangle\cdot\mathbf{t}_{\Gamma_d}d\Gamma - \int_{\Gamma_d} \left(\mathbf{N}_w^{enr}\right)^{\mathrm{T}}[[\dot{\mathbf{u}}]]\cdot\mathbf{n}_{\Gamma_d}d\Gamma \\ -\int_{\Gamma_d} \left(\nabla\mathbf{N}_w^{enr}\right)^{\mathrm{T}}\mathbf{t}_{\Gamma_d}(2h)(k_{wd})\nabla p_w\cdot\mathbf{t}_{\Gamma_d}d\Gamma \\ -\int_{\Gamma_d} \left(\nabla\mathbf{N}_w^{enr}\right)^{\mathrm{T}}\mathbf{t}_{\Gamma_d}(2h)(k_{wd}\rho_w)\langle\ddot{\mathbf{u}}\rangle\cdot\mathbf{t}_{\Gamma_d}d\Gamma \\ +\int_{\Gamma_d} \left(\nabla\mathbf{N}_w^{enr}\right)^{\mathrm{T}}\mathbf{t}_{\Gamma_d}(2h)(k_{wd}\rho_w)\mathbf{b}\cdot\mathbf{t}_{\Gamma_d}d\Gamma \end{bmatrix} \tag{A.10}$$

References

Allen, M.B., Herrera, I., Pinder, G.F., 1988. Numerical Modeling in Science and Engineering. Wiley, New York.

Arzanfudi, M.M., Al-Khoury, R., 2017. Thermo-hydrodynamic-mechanical multiphase flow model for CO2 sequestration in fracturing porous media. Int. J. Numer. Meth. Fluids 84, 635–674.

Bai, Q., Liu, Z., Zhang, C., Wang, F., 2020. Geometry nature of hydraulic fracture propagation from oriented perforations and implications for directional hydraulic fracturing. Comput. Geotech. 125, 103682.

Bazant, Z.P., Planas, J., 1998. Fracture and Size Effect in Concrete and Other Quasibrittle Materials. CRC Press, Boca Raton.

Bažant, Z.P., Salviato, M., Chau, V.T., Viswanathan, H., Zubelewicz, A., 2014. Why fracking works. J. Appl. Mech. 81.

Beroza, G.C., Ide, S., 2009. Deep tremors and slow quakes. Science 324, 1025–1026.

Black, A., 1988. Investigation of lost circulation problems with oil-base drilling fluids. DEA 13 (Phase II). Prepared by Drilling Research Laboratory. Final Report,.

Bunger, A.P., Detournay, E., 2008. Experimental validation of the tip asymptotics for a fluid-driven crack. J. Mech. Phys. Solids 56, 3101–3115.

Bunger, A.P., Gordeliy, E., Detournay, E., 2013. Comparison between laboratory experiments and coupled simulations of saucer-shaped hydraulic fractures in homogeneous brittle-elastic solids. J. Mech. Phys. Solids 61, 1636–1654.

Burlini, L., Di Toro, G., 2008. Volcanic symphony in the lab. Science 322, 207–208.

Burlini, L., Di Toro, G., Meredith, P., 2009. Seismic tremor in subduction zones: Rock physics evidence. Geophys. Res. Lett. 36.

Cao, T.D., Milanese, E., Remij, E.W., Rizzato, P., Remmers, J.J.C., Simoni, L., Huyghe, J. M., Hussain, F., Schrefler, B.A., 2017. Interaction between crack tip advancement and fluid flow in fracturing saturated porous media. Mech. Res. Commun. 80, 24–37.

Chan, A.H.C., Pastor, M., Schrefler, B.A., Shioni, T., Zienkiewicz, O.C., 2022. Computational Geomechanics. John Wiley, Theory and Applications.

Cox, S.F., 1995. Faulting processes at high fluid pressures: an example of fault valve behavior from the Wattle Gully Fault, Victoria, Australia. J. Geophys. Res. Solid Earth 100, 12841–12859.

De Pater, C.J., 2015. Hydraulic fracture containment: New insights into mapped geometry, in: SPE Hydraulic Fracturing Technology Conference. SPE, The Woodlands, Texas.

Detournay, E., 2016. Mechanics of hydraulic fractures. Annu. Rev. Fluid Mech. 48, 311–339.

Ding, J., Remmers, J.J.C., Leszczynski, S., Huyghe, J.M., 2018. Swelling driven crack propagation in large deformation in ionized hydrogel. J. Appl. Mech. 85.

Dong, J., Chen, M., Jin, Y., Hong, G., Zaman, M., Li, Y., 2019. Study on micro-scale properties of cohesive zone in shale. Int. J. Solids Struct. 163, 178–193.

Duan, K., Kwok, C.Y., Zhang, Q., Shang, J., 2020. On the initiation, propagation and reorientation of simultaneously-induced multiple hydraulic fractures. Comput. Geotech. 117, 103226.

Farhat, C., Sobh, N., 1990. A consistency analysis of a class of concurrent transient implicit/explicit algorithms. Comput. Methods Appl. Mech. Eng. 84, 147–162.

Fathima, K.M.P., de Borst, R., 2019. Implications of single or multiple pressure degrees of freedom at fractures in fluid-saturated porous media. Eng. Fract. Mech. 213, 1–20.

Feng, Y., Gray, K.E., 2017. Parameters controlling pressure and fracture behaviors in field injectivity tests: a numerical investigation using coupled flow and geomechanics model. Comput. Geotech. 87, 49–61.

Fisher, K., Warpinski, N., 2012. Hydraulic-fracture-height growth: Real data. SPE Prod. Oper. 27, 8–19.

Fuh, G.-F., Morita, N., Boyd, P.A., McGoffin, S.J., 1992. A new approach to preventing lost circulation while drilling, in: SPE Annual Technical Conference and Exhibition.

Geertsma, J., Haafkens, R., 1979. A comparison of the theories for predicting width and extent of vertical hydraulically induced fractures. J. Energy Res. Technol. 101, 8–19.

Hageman, T., de Borst, R., 2021. Stick-slip like behavior in shear fracture propagation including the effect of fluid flow. Int. J. Numer. Anal. Meth. Geomech. 45, 965–989.

Hageman, T., Fathima, K.M.P., de Borst, R., 2019. Isogeometric analysis of fracture propagation in saturated porous media due to a pressurised non-Newtonian fluid. Comput. Geotech. 112, 272–283.

Herrmann, H.J., 1990. Fracture patterns and scaling laws. Physica A 163, 359–372.

Jafari, A., Vahab, M., Khalili, N., 2021. Fully coupled XFEM formulation for hydraulic fracturing simulation based on a generalized fluid leak-off model. Comput. Methods Appl. Mech. Eng. 373, 113447.

Khoei, A.R., 2015. Extended Finite Element Method. John Wiley, Theory and Applications.

Khoei, A.R., Mortazavi, S.M.S., 2020. Thermo-hydro-mechanical modeling of fracturing porous media with two-phase fluid flow using X-FEM technique. Int. J. Numer. Anal. Meth. Geomech. 44, 2430–2472.

Khoei, A.R., Vahab, M., Haghighat, E., Moallemi, S., 2014. A mesh-independent finite element formulation for modeling crack growth in saturated porous media based on an enriched-FEM technique. Int. J. Fract. 188, 79–108.

Khoei, A.R., Hirmand, M., Vahab, M., Bazargan, M., 2015. An enriched FEM technique for modeling hydraulically driven cohesive fracture propagation in impermeable

media with frictional natural faults: Numerical and experimental investigations. Int. J. Numer. Meth. Eng. 104, 439–468.

Khoei, A.R., Hosseini, N., Mohammadnejad, T., 2016a. Numerical modeling of two-phase fluid flow in deformable fractured porous media using the extended finite element method and an equivalent continuum model. Adv. Water Resour. 94, 510–528.

Khoei, A.R., Vahab, M., Hirmand, M., 2016b. Modeling the interaction between fluid-driven fracture and natural fault using an enriched-FEM technique. Int. J. Fract. 197, 1–24.

Khoei, A.R., Vahab, M., Hirmand, M., 2018. An enriched–FEM technique for numerical simulation of interacting discontinuities in naturally fractured porous media. Comput. Methods Appl. Mech. Eng. 331, 197–231.

Kresse, O., Cohen, C., Weng, X., Wu, R., Gu, H., 2011. Numerical modeling of hydraulic fracturing in naturally fractured formations, in: 45th US Rock Mechanics/Geomechanics Symposium.

Lecampion, B., Bunger, A., Zhang, X., 2018. Numerical methods for hydraulic fracture propagation: a review of recent trends. J. Nat. Gas Sci. Eng. 49, 66–83.

Lewis, R.W., Schrefler, B.A., 1998. The Finite Element Method in the Static and Dynamic Deformation and Consolidation of Porous Media. John Wiley.

Lhomme, T.P., 2005. Initiation of hydraulic fractures in natural sandstones. Delft University of Technology, TU Delft.

Lhomme, T.P., de Pater, C.J., Helfferich, P.H., 2002. Experimental study of hydraulic fracture initiation in Colton sandstone, in: SPE/ISRM Rock Mechanics Conference.

Liang, Z.Z., Xing, H., Wang, S.Y., Williams, D.J., Tang, C.A., 2012. A three-dimensional numerical investigation of the fracture of rock specimens containing a pre-existing surface flaw. Comput. Geotech. 45, 19–33.

Miehe, C., Mauthe, S., Teichtmeister, S., 2015. Minimization principles for the coupled problem of Darcy-Biot type fluid transport in porous media linked to phase field modeling of fracture. J. Mech. Phys. Solids 82, 186–217.

E. Milanese, E., Yilkmaz, O., Molinari J.-F., B. A. Schrefler, B.A., 2016. Avalanches in dry and saturated disordered media at fracture, Phys. Rev. E 93, 4, 043002.

Moës, N., Belytschko, T., 2002. Extended finite element method for cohesive crack growth. Eng. Fract. Mech. 69, 813–833.

Mohammadnejad, T., Khoei, A.R., 2013a. Hydro-mechanical modeling of cohesive crack propagation in multiphase porous media using the extended finite element method. Int. J. Numer. Anal. Meth. Geomech. 37, 1247–1279.

Mohammadnejad, T., Khoei, A.R., 2013b. An extended finite element method for hydraulic fracture propagation in deformable porous media with the cohesive crack model. Finite Elem. Anal. Des. 73, 77–95.

Morita, N., Black, A.D., Guh, G.F., 1990. Theory of lost circulation pressure. in: SPE Annual Technical Conference and Exhibition.

Morris, J.L., 1983. Computational Methods in Elementary Numerical Analysis. Wiley, Chichester.

Nguyen, V.P., Lian, H., Rabczuk, T., Bordas, S., 2017. Modelling hydraulic fractures in porous media using flow cohesive interface elements. Eng. Geol. 225, 68–82.

Ni, T., Pesavento, F., Zaccariotto, M., Galvanetto, U., Schrefler, B.A., 2021. Numerical simulation of forerunning fracture in saturated porous solids with hybrid FEM/Peridynamic model. Comput. Geotech. 133, 104024.

O`Keeffe, N., 2019. Fluid-driven fractures in elastic hydrogels: propagation and coalescence. University of Cambridge.

O`Keeffe, N.J., Zheng, Z., Huppert, H.E., Linden, P.F., 2018. Symmetric coalescence of two hydraulic fractures. Proc. Natl. Acad. Sci. 115, 10228–10232.

Obara, K., Hirose, H., Yamamizu, F., Kasahara, K., 2004. Episodic slow slip events accompanied by non-volcanic tremors in southwest Japan subduction zone. Geophys. Res. Lett. 31.

Okland, D., Gabrielsen, G.K., Gjerde, J., Koen, S., Williams, E.L., 2002. The importance of extended leak-off test data for combatting lost circulation, in: SPE/ISRM Rock Mechanics Conference.

Ortega, J.M., Rheinboldt, W.C., 1970. Iterative Solution of Nonlinear Equations in Several Variables. Academic Press, San Diego.

Peruzzo, C., Cao, D.T., Milanese, E., Favia, P., Pesavento, F., Hussain, F., Schrefler, B.A., 2019a. Dynamics of fracturing saturated porous media and self-organization of rupture. European Journal of Mechanics-A/Solids 74, 471–484.

Peruzzo, C., Simoni, L., Schrefler, B.A., 2019b. On stepwise advancement of fractures and pressure oscillations in saturated porous media. Eng. Fract. Mech. 215, 246–250.

Phillips, W.J., 1972. Hydraulic fracturing and mineralization. J. Geol. Soc. London 128, 337–359.

Pizzocolo, F., Huyghe, J.M., Ito, K., 2013. Mode I crack propagation in hydrogels is step wise. Eng. Fract. Mech. 97, 72–79.

Razavi, O., Vajargah, A.K., van Oort, E., Aldin, M., Govindarajan, S., 2016. Optimization of wellbore strengthening treatment in permeable formations, in: SPE Western Regional Meeting.

Réthoré, J., De Borst, R., Abellan, M.A., 2008. A two-scale model for fluid flow in an unsaturated porous medium with cohesive cracks. Comput. Mech. 42, 227–238.

Richtmyer, R.D., Morton, K.W., 1967. Difference Methods for Initial-Value Problems. New York.

Sammonds, P.R., Meredith, P.G., Ayling, M.R., Jones, C., Murrell, S.A.F., 1989. Acoustic measurements during fracture of triaxially deformed rock. In: Fracture of Concrete and Rock: Rcent Developments. University of Wales, Cardiff, Society of Automotive Engineers.

Schrefler, B.A., Secchi, S., Simoni, L., 2006. On adaptive refinement techniques in multi-field problems including cohesive fracture. Comput. Methods Appl. Mech. Eng. 195, 444–461.

Schwartz, S.Y., Rokosky, J.M., 2007. Slow slip events and seismic tremor at circum-Pacific subduction zones. Rev. Geophys. 45.

Shi, F., Liu, J., 2021. A fully coupled hydromechanical XFEM model for the simulation of 3D non-planar fluid-driven fracture propagation. Comput. Geotech. 132, 103971.

Sibson, R.H., 1994. Crustal stress, faulting and fluid flow. Geological Society 78, 69–84.

Slepyan, L., Ayzenberg-Stepanenko, M., Mishuris, G., 2015. Forerunning mode transition in a continuous waveguide. J. Mech. Phys. Solids 78, 32–45.

Soliman, M.Y., Wigwe, M., Alzahabi, A., Pirayesh, E., Stegent, N., 2014. Analysis of fracturing Pressure data in heterogeneous shale formations. Texas Tech University.

Sun, Y., Chen, B., Edwards, M.G., Li, C., 2021b. Investigation of hydraulic fracture branching in porous media with a hybrid finite element and peridynamic approach. Theor. Appl. Fract. Mech. 116, 103133.

Sun, W., Fish, J., Ni, P., 2021a. Superposition-based concurrent multiscale approaches for poromechanics. Int. J. Numer. Meth. Eng. 122, 7328–7353.

Trimonova, M., Baryshnikov, N., Zenchenko, E., Zenchenko, P., Turuntaev, S., 2017. The study of the unstable fracure propagation in the injection well: Numerical and laboratory modeling, in: SPE Russian Petroleum Technology Conference.

Turska, E., Schrefler, B., 1993. On convergence conditions of partitioned solution procedures for consolidation problems. Comput. Methods Appl. Mech. Eng. 106, 51–63.

Tvergaard, V., Needleman, A., 1993. An analysis of the brittle-ductile transition in dynamic crack growth. Int. J. Fract. 59, 53–67.

Tzschichholz, F., Herrmann, H.J., 1995. Simulations of pressure fluctuations and acoustic emission in hydraulic fracturing. Phys. Rev. E 51, 1961.

Vahab, M., Akhondzadeh, S., Khoei, A.R., Khalili, N., 2018. An X-FEM investigation of hydro-fracture evolution in naturally-layered domains. Eng. Fract. Mech. 191, 187–204.

Vahab, M., Khalili, N., 2017. Numerical investigation of the flow regimes through hydraulic fractures using the X-FEM technique. Eng. Fract. Mech. 169, 146–162.

Wilson, Z.A., Landis, C.M., 2016. Phase-field modeling of hydraulic fracture. J. Mech. Phys. Solids 96, 264–290.

Zhang, G.Q., Chen, M., 2010. Dynamic fracture propagation in hydraulic re-fracturing. J. Pet. Sci. Eng. 70, 266–272.

Zhang, Q., Zhang, X.-P., Ji, P.Q., 2019. Numerical study of interaction between a hydraulic fracture and a weak plane using the bonded-particle model based on moment tensors. Comput. Geotech. 105, 79–93.

Zhou, Y., Yang, D., 2022. A fast simulation method for hydraulic-fracture-network generation in fractured rock based on fully coupled XFEM. Comput. Geotech. 150, 104892.

Zhou, S., Zhuang, X., Rabczuk, T., 2018. A phase-field modeling approach of fracture propagation in poroelastic media. Eng. Geol. 240, 189–203.

Zienkiewicz, O.C., Chang, C.T., Bettess, P., 1980. Drained, undrained, consolidating and dynamic behaviour assumptions in soils. Geotechnique 30, 385–395.

Zou, J., Jiao, Y.Y., Tang, Z., Ji, Y., Yan, C., Wang, J., 2020. Effect of mechanical heterogeneity on hydraulic fracture propagation in unconventional gas reservoirs. Comput. Geotech. 125, 103652.